

Constraining models of the pulsar wind nebula in SNR G0.9+0.1 via simulation of its detection properties using the Cherenkov Telescope Array

M. Fiori^{1,2★}, L. Zampieri^{1,2★}, A. Burtovoi^{1,2,3}, P. Caraveo⁴ and L. Tibaldo⁵

¹Department of Physics and Astronomy, University of Padova, Via F. Marzolo 8, I-35131, Padova, Italy

²INAF, Osservatorio Astronomico di Padova, Vicolo dell'Osservatorio 5, I-35122, Padova, Italy

³Centre of Studies and Activities for Space (CISAS) 'G. Colombo', University of Padova, Via Venezia 15, I-35131, Padova, Italy

⁴INAF-IASF Milano, Via A. Corti 12, I-20133, Milano, Italy

⁵IRAP, Université de Toulouse, CNRS, CNES, UPS, 9 avenue Colonel Roche, F-31028 Toulouse, Cedex 4, France

Accepted 2020 September 28. Received 2020 September 28; in original form 2020 May 15

ABSTRACT

SNR G0.9+0.1 is a well-known source in the direction of the Galactic Centre composed by a Supernova Remnant (SNR) and a Pulsar Wind Nebula (PWN) in the core. We investigate the potential of the future Cherenkov Telescope Array (CTA), simulating observations of SNR G0.9 + 0.1. We studied the spatial and spectral properties of this source and estimated the systematic errors of these measurements. The source will be resolved if the very high-energy emission region is bigger than $\sim 0.65'$. It will also be possible to distinguish between different spectral models and calculate the cutoff energy. The systematic errors are dominated by the Instrument Response Function instrumental uncertainties, especially at low energies. We computed the evolution of a young PWN inside an SNR using a one-zone time-dependent leptonic model. We applied the model to the simulated CTA data and found that it will be possible to accurately measure the cutoff energy of the γ -ray spectrum. Fitting of the multiwavelength spectrum will allow us to constrain also the magnetization of the PWN. Conversely, a pure power-law spectrum would rule out this model. Finally, we checked the impact of the spectral shape and the energy density of the Inter-Stellar Radiation Fields on the estimate of the parameters of the PWN, finding that they are not significantly affected.

Key words: instrumentation: detectors – supernovae: individual: SNR G0.9+0.1 – ISM: supernova remnants – gamma-rays: general.

1 INTRODUCTION

Pulsar Wind Nebulae (PWNe) represent the most numerous class of identified Galactic Very High Energy (VHE) γ -ray sources (de Oña-Wilhelmi et al. 2013). These objects are highly magnetized nebulae powered by young and energetic pulsars. Inside these nebulae, non-thermal radiation up to ~ 100 TeV is produced (Rieger, de Oña-Wilhelmi & Aharonian 2013).

In young PWNe, the outer radius of the nebula has not yet started to interact with the reverse shock of the Supernova Remnant (SNR). Therefore, they are particularly interesting objects because the uncertainties related to the interaction are not present and their evolution can be fairly well reproduced by physical models. These models can thus be tested against observations, providing important information on the physical processes at work in these sources (e.g. Gelfand, Slane & Zhang 2009; Martín, Torres & Rea 2012; Zhu, Fang & Zhang 2015).

The Cherenkov Telescope array (CTA, Actis et al. 2011) will be capable to study the γ -ray emission of PWNe in great detail. With CTA, it will be possible to observe PWNe from few GeV up to hundreds of TeV, accurately sampling most of the Inverse-Compton (IC) peak as well as obtaining a measurement of the spectral cutoff energies where present. In addition, the unprecedented

angular resolution will allow us to determine more precisely the γ -ray emission regions and to investigate the existence of any potential energy-dependent morphology. Thanks to this, it will be possible to test various γ -ray emission models of PWNe and to better understand their magnetohydrodynamic structure and evolution.

The purpose of this work is testing the capabilities of CTA in connection with a specific source (SNR G0.9+0.1) while, at the same time, assessing the impact of CTA observations on our understanding of the physical processes occurring in PWNe. The source selected is SNR G0.9 + 0.1 (at TeV energies, the source is also referred as HESS J1747-281; H. E. S. S. Collaboration 2018a), a well-known composite Supernova Remnant (SNR, Helfand & Becker 1987). The bright central core has been unambiguously identified as a PWN through X-ray observations (Gaensler, Pivovarov & Garmire 2001). SNR G0.9 + 0.1 is composed by a PWN in the core (with a diameter of $\sim 2'$) surrounded by an SNR (with a diameter of $\sim 8'$, Dubner, Giacani & Decourchelle 2008). This source has been detected at VHE by HESS (Aharonian et al. 2005), VERITAS (Smith & the VERITAS Collaboration 2015), and MAGIC (Ahnen et al. 2017) only up to ~ 20 TeV, without any evidence of a cutoff at TeV energies. Moreover, for all these facilities, the source appears point-like because of the limited angular resolution.

SNR G0.9 + 0.1 is considered to be a young PWN with an estimated age of ~ 2000 – 3000 yr (Sidoli et al. 2000; Camilo et al. 2009). Due to the projected position of the source, in the direction of the Galactic Centre, and the uncertainties in the electron density

* E-mail: michele.fiori86@gmail.com (MF); luca.zampieri@inaf.it (LZ)

model in that direction, the distance is not well determined (between 8 and 16 kpc, as suggested by Camilo et al. 2009). SNR G0.9 + 0.1 has been often adopted as a benchmark to test various theoretical models (e.g. Venter & de Jager 2007; Qiao, Zhang & Fang 2009; Fang & Zhang 2010; Tanaka & Takahara 2011; Torres et al. 2014; van Rensburg, Krüger & Venter 2018; Zhu, Zhang & Fang 2018). In the early studies of Venter & de Jager (2007) and Qiao et al. (2009), only an approximate treatment of the energy losses was included, while the dynamical evolution of the nebula was not considered. Fang & Zhang (2010) incorporated the dynamical evolution of the nebula but assumed an injection spectrum for the electrons in the form of a Maxwellian plus a power-law tail, instead of the most widely adopted broken power law (as in Tanaka & Takahara 2011, Torres et al. 2014, and Zhu et al. 2018). More recently, van Rensburg et al. (2018) presented a more accurate multizone time-dependent leptonic model to reproduce the spatial properties of the source. In this paper, we did not focus on modelling in detail the energy-dependent morphology of SNR G0.9 + 0.1 (the angular resolution at VHE is not sufficient to do it) but adopted a one-zone time-dependent leptonic model, even if it has been shown that lower energy observations with a better angular resolution would benefit from multizone models (see e.g. van Rensburg et al. 2018; Lu et al. 2019; van Rensburg et al. 2020). Following Torres et al. (2014) and Zhu et al. (2018), we considered the evolution of a single population of accelerated electrons inside an expanding uniform medium in spherical symmetry. This approach turned out to be sufficiently accurate for reproducing the multiwavelength (MWL) emission of the PWN and allowed us to make predictions on the spectrum of SNR G0.9 + 0.1 at the highest energies.

Similarly, we used SNR G0.9 + 0.1 as a test case to demonstrate the improvements that the CTA South array will allow us to achieve. The source position, its faintness (only about 2 per cent of the Crab flux), and the small angular size make this object a really interesting target for testing the capabilities of the CTA. Since the extension of the PWN in SNR G0.9 + 0.1 is comparable to the best angular resolution achievable with CTA, we expect to be able to measure its size at VHEs. A measurement of the angular size of the source is needed to better constrain the physical models and to compare the source size at different wavelengths. This would help understanding if the VHE emission comes from the central source or if there is some contribution from the SNR shell. In addition, the sensitivity of CTA will be much better up to and above 100 TeV (CTA Consortium 2019), allowing us to measure a possible cutoff at energies higher than 20 TeV (not excluded with the currently available data). Also, this measurement is important to better constrain the physical models of the nebula, since it will constrain the particle injection spectrum and specifically the maximum energy of the electrons (assuming a leptonic model). At such high energies, the inverse Compton emission may be in the Klein–Nishina regime, and thus obtaining such a measurement will be a very good proxy of the actual maximal electron energy. This in turn may constrain the acceleration process at the PWN termination shock.

In this work, we present a comprehensive study of the spatial and spectral properties of SNR G0.9+0.1 aiming at testing the observability of specific features in the simulated data, studying the spatial extension of the TeV emission and the presence of a VHE cutoff in the spectrum, and comparing the data to models of the MWL spectrum. Furthermore, we estimate the systematic uncertainties that may affect observations of SNR G0.9 + 0.1 carried out with CTA.

This paper is organized as follows. In Section 2, we describe the models and the analysis of the spatial and spectral properties of SNR G0.9 + 0.1 as seen by CTA. In Section 3, we report the results of the

simulations. In Section 4, we estimate the systematic uncertainties and in Section 5, we discuss the results of our analysis. In Section 6, we describe the implementation of a physical model for the emission of a young PWN inside an SNR. Finally, in Section 7, we discuss our results and compare the numerical solutions with the simulations of the CTA observations of SNR G0.9 + 0.1.

2 SIMULATIONS

To simulate, reduce, and analyse the γ -ray data, we made use of the software *ctools*, a software package developed for the scientific analysis of CTA data (Knödlseeder et al. 2016).

We specified in input: a spatial and a spectral model describing the emission region of SNR G0.9 + 0.1 and a model for the spatial distribution of the cosmic ray background. For the spectral models, we adopted both a power law and a power law with an exponential cutoff (PLEC):

$$\frac{dN}{dE} = N_0 \left(\frac{E}{E_0} \right)^{-\Gamma}, \quad (1)$$

$$\frac{dN}{dE} = N_0 \left(\frac{E}{E_0} \right)^{-\Gamma} \exp\left(-\frac{E}{E_{\text{cut}}}\right), \quad (2)$$

where N_0 is a normalization factor, Γ the spectral index, E_0 the pivot energy, and E_{cut} the cutoff energy. For the spatial model, we use different distributions as described in the following.

SNR G0.9+0.1 is projected in the direction of the crowded region of the Galactic Centre. In order to understand which sources can significantly affect the measurement of the flux of SNR G0.9 + 0.1 and to test the capability of *ctools* in reproducing the extended emission of the Galactic Centre, we simulate the γ -ray emission in a field of $3^\circ \times 1^\circ$ around the position of Sgr A*. In doing that, we take into account all the known TeV sources and the diffuse emission in the direction of the Galactic Centre, as outlined below.

2.1 Galactic Centre extended region

In a box of 3 square degrees around the centre of the Galaxy, there are many sources at TeV energies as observed by the HESS, MAGIC, and VERITAS collaborations (Aharonian et al. 2006a; Archer et al. 2016; H. E. S. S. Collaboration et al. 2017; Ahnen et al. 2017).

We consistently selected all the sources from the HESS catalogue,¹ except for SNR G0.9 + 0.1 for which we considered all the data included in a joint HESS+VERITAS² analysis of the source (Smith & the VERITAS Collaboration 2015).³ The sources considered in our simulation are listed below and their spatial and spectral parameters are reported in Table 1.

(i) HESS J1745-290 (Aharonian et al. 2004): This source represents the TeV emission coming from the centre of our Galaxy (Acero et al. 2010). It is associated with the supermassive black hole Sgr A* or to the candidate PWN G359.95-0.04 (Kistler 2015). It is modelled as a point source with a power-law spectrum with an exponential cutoff. The spectral parameters are taken from Aharonian et al. (2009)

(ii) HESS J1741-302 (Tibolla et al. 2008): It is an unidentified source detected with HESS at ~ 1 per cent of the Crab flux above 1 TeV. We modelled it as a point source with a power-law spectrum.

¹www.mpi-hd.mpg.de/hfm/HESS/pages/home/sources/

²veritas.sao.arizona.edu/

³The results of the analysis on the sole HESS data (Aharonian et al. 2005) are consistent with the results of the joint analysis.

Table 1. Input data used with *ctobssim* to simulate the VHE emission from a region of $\approx 3^\circ \times 1^\circ$ around the Galactic Centre. The reported positions are taken from the SIMBAD astronomical data base (Wenger et al. 2000), except for the position of the Galactic diffuse emission for which we adopt the position of the centre of the template map. E_0 is always equal to 1 TeV.

Source	Spatial model	Position	Spectral model	Input parameters
HESS J1745-290	Point source	RA = 266°4150 Dec = -29°0061	PLEC ^d	$N_0 = 2.55 \times 10^{-12} \text{ TeV}^{-1} \text{ cm}^{-2} \text{ s}^{-1}$ $\Gamma = 2.10$ $E_{\text{cut}} = 15.7 \text{ TeV}$
HESS J1741-302	Point source	RA = 265°2500 Dec = -30°2000	Power law ^e	$N_0 = 2.34 \times 10^{-13} \text{ TeV}^{-1} \text{ cm}^{-2} \text{ s}^{-1}$ $\Gamma = 2.30$
HESS J1745-303	Extended source HESS excess map ^a	RA = 266°2970 Dec = -30°1990	Power law ^f	$N_0 = 2.84 \times 10^{-12} \text{ TeV}^{-1} \text{ cm}^{-2} \text{ s}^{-1}$ $\Gamma = 2.71$
Galactic Diffuse	Extended source HESS excess map ^b	RA = 266°6518 Dec = -28°7166	Power law ^g	$N_0 = 1.73 \times 10^{-8} \text{ TeV}^{-1} \text{ cm}^{-2} \text{ s}^{-1} \text{ sr}^{-1}$ $\Gamma = 2.29$
SNR G0.9 + 0.1	Extended source SUMSS radiomap (843 MHz) ^c	RA = 266°8250 Dec = -28°1500	Power law ^h	$N_0 = 8.80 \times 10^{-13} \text{ TeV}^{-1} \text{ cm}^{-2} \text{ s}^{-1}$ $\Gamma = 2.30$

Notes. ^aFig. 1. ^bFig. 2. ^cFig. 3.

^dAharonian et al. (2009). ^eTibolla et al. (2008). ^fAharonian et al. (2008). ^gAharonian et al. (2006a). ^hSmith & the VERITAS Collaboration (2015).

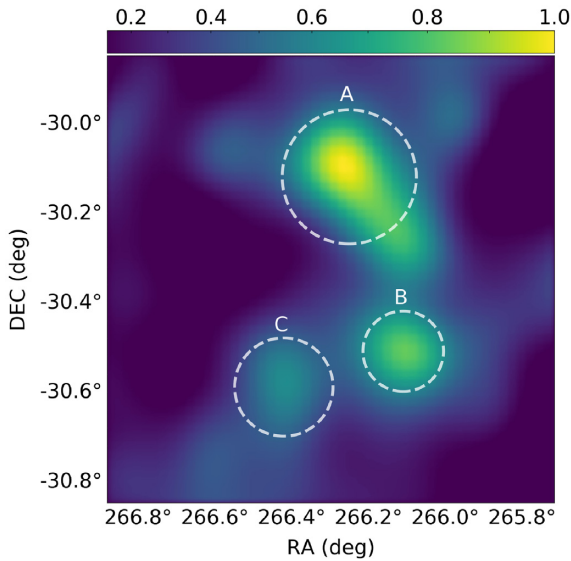


Figure 1. Excess map of HESS J1745-303 (Aharonian et al. 2008), used as spatial model for our simulations. The three dashed circles indicate the positions of the brightest emitting regions of the source.

(iii) HESS J1745-303 (Aharonian et al. 2006b): This is an extended and unidentified VHE γ -ray source at a Galactic longitude of -0.4° . The morphology of the source is quite complex owing to the presence of three major emitting regions. The spatial extension of this source has been modelled using the HESS excess map,⁴ shown in Fig. 1.

The spectral model is a power law (Aharonian et al. 2008).

(iv) Diffuse emission along the Galactic plane (Aharonian et al. 2006a): It is a region of diffuse emission (of approximately $\pm 1^\circ$ in galactic longitude) probably associated with the interaction of cosmic ray particles with molecular clouds and that contains a number of unidentified sources such as, for example HESS J1746-285 (H. E. S. S. Collaboration 2017). This diffuse emission is the only source that can affect our simulation of SNR G0.9 + 0.1 because the spatial

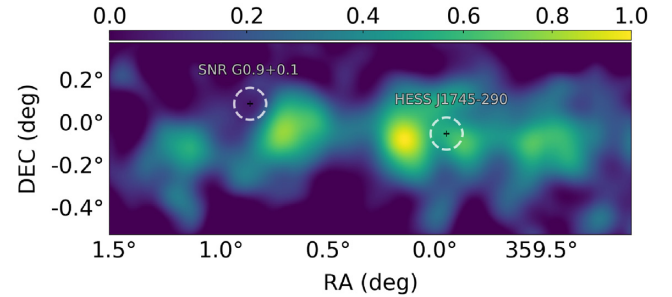


Figure 2. HESS excess map of the diffuse emission around the Galactic Centre (the emission from SNR G0.9 + 0.1 and HESS J1745-290 has been previously subtracted) (Aharonian et al. 2006a), used as input spatial model for our simulations.

emission regions of these sources overlap. For the spatial model, we used a section (between $359.1^\circ < l < 1.5^\circ$ and $|b| < 0.4^\circ$, in Galactic coordinates) of an image taken from HESS⁵ (Fig. 2) in which the emission coming from HESS J1745-290 and SNR G0.9 + 0.1 has been previously subtracted. The spectral model is a power law.

(v) SNR G0.9 + 0.1 (Aharonian et al. 2005): The spatial model is taken from a radiomap at 843 MHz from the Sydney University Molonglo Sky Survey⁶ (radiomap template hereafter). The map has been prepared for the simulation with a technique developed for the analysis of extended sources in *Fermi*-LAT.⁷ For the spectral model, we used a single power law for the entire system, as assumed for the HESS and VERITAS observations (Smith & the VERITAS Collaboration 2015) since from currently available data, it is not possible to discriminate between the emission coming from the PWN and the SNR.

To simulate observations of the field with the southern CTA facility (CTA-South), we made use of the Instrument Response Functions (IRFs) of the baseline array made available by the CTA Consortium (Acharyya et al. 2019). We provided as input all the information on the sources listed above, plus a model for the spatial distribution of

⁴www.mpi-hd.mpg.de/hfm/HESS/pages/publications/auxiliary/hessj1745-303-aux.html

⁵www.mpi-hd.mpg.de/hfm/HESS/pages/publications/auxiliary/gcdiffuse_auxinfo.html

⁶skyview.gsfc.nasa.gov/surveys/sumss/mosaics/Galactic/J1752M28.FITS

⁷fermi.gsfc.nasa.gov/ssc/data/analysis/scitools/extended/extended.html

the cosmic ray background ('CTAIrfBackground'). We simulated four observations with different observing times centred on the position of Sgr A* in the energy range of 0.2–180 TeV: one 30-min observation, one 5-h observation, one 50-h observation, and one 200-h observation. We simulated observations lasting up to 200 h because we wanted to test the results achievable with CTA under the best assumptions regarding the observing time. This number is justified by the fact that the Galactic Centre will be extensively observed during the first years of CTA operations (CTA Consortium 2019). We then made an unbinned analysis⁸ and fitted all the simulated data with the same models given in input. Applying the maximum likelihood method, we finally compute the Test Statistics (TS) value for each source.⁹

2.2 SNR G0.9 + 0.1

As far as SNR G0.9+0.1 is concerned, we divided the analysis in two parts: first we fixed all the spectral parameters of the source and varied only the spatial model and then we kept fixed the spatial model (one of the previously selected models) and varied the spectral parameters. At this stage, we include in the simulations only the information on SNR G0.9 + 0.1, the diffuse emission from the Galactic plane, and the cosmic ray background. The simulated field has a radius of 0.25° centred on the source.

To understand the capabilities of CTA in resolving the spatial extension of the VHE emission of SNR G0.9 + 0.1, we perform the simulations using different spatial models in the energy range of 0.2–180 TeV. All the simulated observations last 200 h and have fixed spectral parameters (a power law with the parameters reported in Table 1). The spatial models used here are: point source (assuming that the VHE emission comes only from the inner part of the remnant), a radiomap template (assuming that the VHE emission comes from the same region as the radio emission), and various spatially uniform radial disc models with different radii, from 1 arcsec to 90 arcsec. We then fit all the simulated data with four different spatial models: a point source model, a radial Gaussian model, a radial disc model, and the radiomap template model. Model fitting has been performed with a binned maximum likelihood analysis¹⁰ (binned cube centred on source position with 0.01° pixel size bin, 2500 pixel, gnomonic projection, and 100 logarithmic energy bins). At this stage, we adopted the binned analysis because, for long exposures, the computation time is much shorter than with the unbinned analysis.

After the analysis of the spatial properties of the source, we perform the analysis of the spectral properties fixing all the spatial parameters. Our goal is to assess the detectability of the source in the higher energy range (from 30 TeV up to 180 TeV) and the capability of CTA-South to distinguish between different spectral models. We simulate different observations, all lasting 200 h, with the source spatially modelled with the radiomap template and spectrally modelled with a power law and various PLEC with different cutoff energies (20 TeV, 30 TeV, 50 TeV, and 100 TeV). Data are simulated in the energy range between 0.2 TeV and 180 TeV. Model fitting has been performed with the binned likelihood analysis. The spectral energy distribution (SED) of the source is extracted using *csspec*, a specific tool of ctools.

3 SIMULATIONS RESULTS

3.1 Galactic Centre extended region

In Table 2, we show the results of the unbinned analysis performed on the four different simulations of the Galactic Centre region mentioned in Section 2.1. We report all the TS values and the spectral parameters measured for all the sources in the simulations. These measurements were performed to check the detectability of all the simulated sources and to determine the needed observing time to reliably recover all the parameters of the sources. After 30 min of observation, all the sources are significantly detected and, as expected, the significance grows increasing the observing time. Already at 50 h, the inferred parameters are in good agreement with the input ones. At 200 h, the inferred parameters are very close to the simulated ones and the associated errors become very small. Therefore, a 200-h observation would lead to the accuracy on the measured parameters of SNR G0.9 + 0.1 needed for the analysis reported below.

We then compared the simulation obtained for an exposure of 50 h with that obtained with HESS in 55 h¹¹ (Aharonian et al. 2006a) in a similar energy range (see Fig. 4). The images are in good agreement, with the CTA simulated one having a lower background contamination. With the same observing time, CTA will allow us to obtain a wider spectral coverage and a higher signal-to-noise ratio.

3.2 SNR G0.9 + 0.1

We performed two different analyses to investigate the resolving capabilities of CTA. In the first analysis, we carry out different fits of the image simulated using the radiomap template. The fits were performed with four different spatial models: point source model, spatially uniform radial disc model (with the radius left free during the fit), radial Gaussian model (with width left free during the fit), and the radiomap model. The results are shown in Fig. 5. If the VHE emission follows the radio emission, CTA could be able to detect the source as an extended object because the TS value for the point source fit is significantly lower. The extended models have similar TS values, with the radiomap template being slightly more significant, indicating that all the three models can reproduce well the simulated data and that the VHE γ -ray emission from outside the PWN (i.e. the emission coming from the SNR shell that can be seen in Fig. 3) is almost negligible.

In the second analysis, we test the limiting resolving capabilities of CTA against the background of the Galactic Centre VHE emission region following the procedure developed to detect an extended source in the *Fermi*-LAT data (Lande et al. 2012). We have simulated different images assuming a spatially uniform radial disc with different radii. We then fit all the images with a point source model and a radial disc model with the radius free to vary. This procedure is then repeated for 100 times to account for the statistical fluctuations that can arise from different simulations.¹² For all the simulated images, we compute the significance of detecting significant spatial extension for the source by using the likelihood ratio test:

$$TS_{\text{ext}} = -2 \log \frac{\mathcal{L}_{\text{RD}}}{\mathcal{L}_{\text{PS}}}, \quad (3)$$

¹¹ www.mpi-hd.mpg.de/hfm/HESS/pages/publications/auxiliary/gcdiffuse_auxinfo.html

¹² Different simulations are based on a different random seed for the Monte Carlo generator that samples the input source models to produce observed photon energies and arrival directions. This is achieved through the random number generator provided in the GammaLib library (Knödlseder et al. 2016).

⁸ <http://cta.irap.omp.eu/ctools/users/tutorials/quickstart/unbinned.html>

⁹ The square root of the TS value is roughly the Gaussian σ in the case of one free parameter associated to the source (see e.g. Protassov et al. 2002).

¹⁰ <http://cta.irap.omp.eu/ctools/users/tutorials/quickstart/fitting.html>

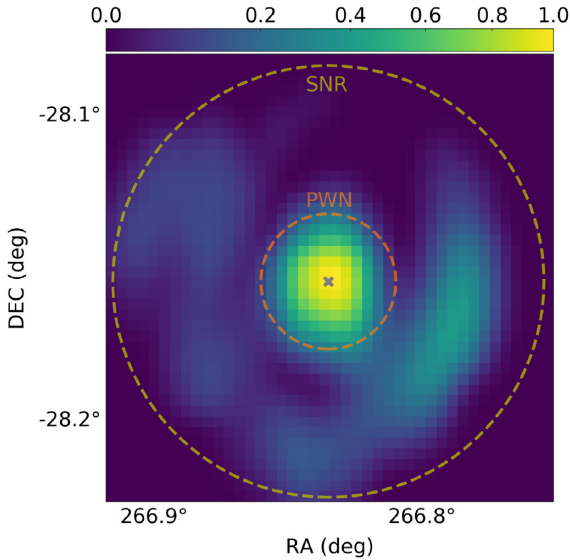
Table 2. Results of the unbinned maximum likelihood analysis on the simulated observations of the Galactic Centre region. After 30 min of observation, all the sources are significantly detected.

Source	0.5-h observation		5-h observation	
	Spectral parameters ^{a,b}	TS	Spectral parameters ^{a,b}	TS
HESS J1745-290	$N_0 = (3.29 \pm 0.47) \times 10^{-12}$ $\Gamma = 1.95 \pm 0.12$ $E_{\text{cut}} = 5.73 \pm 2.06$	371	$N_0 = (2.51 \pm 0.11) \times 10^{-12}$ $\Gamma = 2.07 \pm 0.04$ $E_{\text{cut}} = 14.54 \pm 3.53$	3444
HESS J1741-302	$N_0 = (2.36 \pm 0.74) \times 10^{-13}$ $\Gamma = 2.32 \pm 0.29$	27	$N_0 = (2.55 \pm 0.26) \times 10^{-13}$ $\Gamma = 2.21 \pm 0.07$	301
HESS J1745-303	$N_0 = (2.49 \pm 0.28) \times 10^{-12}$ $\Gamma = 2.83 \pm 0.08$	318	$N_0 = (2.73 \pm 0.09) \times 10^{-12}$ $\Gamma = 2.71 \pm 0.02$	3081
Galactic Diffuse	$N_0 = (1.86 \pm 0.06) \times 10^{-8} \text{sr}^{-1}$ $\Gamma = 2.31 \pm 0.03$	869	$N_0 = (1.71 \pm 0.01) \times 10^{-8} \text{sr}^{-1}$ $\Gamma = 2.30 \pm 0.01$	7787
SNR G0.9 + 0.1	$N_0 = (7.66 \pm 1.32) \times 10^{-13}$ $\Gamma = 2.13 \pm 0.11$	103	$N_0 = (8.12 \pm 0.41) \times 10^{-13}$ $\Gamma = 2.31 \pm 0.04$	995

	50-h observation		200-h observation	
	Spectral parameters ^{a,b}	TS	Spectral parameters ^{a,b}	TS
HESS J1745-290	$N_0 = (2.61 \pm 0.03) \times 10^{-12}$ $\Gamma = 2.07 \pm 0.01$ $E_{\text{cut}} = 13.75 \pm 0.86$	36493	$N_0 = (2.53 \pm 0.01) \times 10^{-12}$ $\Gamma = 2.10 \pm 0.01$ $E_{\text{cut}} = 15.83 \pm 0.53$	142506
HESS J1741-302	$N_0 = (2.36 \pm 0.08) \times 10^{-13}$ $\Gamma = 2.27 \pm 0.03$	2526	$N_0 = (2.38 \pm 0.04) \times 10^{-13}$ $\Gamma = 2.30 \pm 0.01$	9987
HESS J1745-303	$N_0 = (2.79 \pm 0.03) \times 10^{-12}$ $\Gamma = 2.72 \pm 0.07$	32853	$N_0 = (2.83 \pm 0.01) \times 10^{-12}$ $\Gamma = 2.71 \pm 0.01$	132875
Galactic Diffuse	$N_0 = (1.73 \pm 0.01) \times 10^{-8} \text{sr}^{-1}$ $\Gamma = 2.28 \pm 0.03$	80674	$N_0 = (1.73 \pm 0.01) \times 10^{-8} \text{sr}^{-1}$ $\Gamma = 2.29 \pm 0.01$	322679
SNR G0.9 + 0.1	$N_0 = (8.87 \pm 0.13) \times 10^{-13}$ $\Gamma = 2.30 \pm 0.01$	11274	$N_0 = (8.83 \pm 0.06) \times 10^{-13}$ $\Gamma = 2.30 \pm 0.01$	44901

Notes. ^a N_0 in unit of $\text{TeV}^{-1} \text{cm}^{-2} \text{s}^{-1}$ and E_{cut} in unit of TeV. $E_0 = 1 \text{TeV}$.

^bStatistical error only.

**Figure 3.** Radio image (843 MHz) of SNR G0.9 + 0.1 taken from the Sydney University Molonglo Sky Survey (SUMSS) and used as template for some of our simulations. Most of the power in the radio band is coming from the PWN that is surrounded by the less energetic shell of the supernova remnant.

where \mathcal{L}_{RD} and \mathcal{L}_{PS} are the likelihood values of the fits with the radial disc and the point source models. In Fig. 6, we show TS_{ext} in function of the simulated source radius with the 95 per cent confidence level errors. The value increases from very small to large radii, showing that the radial disc model has a significantly better likelihood (TS_{ext}

≥ 25) when the source has a radius larger than 39_{-8}^{+9} arcsec. This means that if the VHE emission region of SNR G0.9 + 0.1 is bigger than ~ 0.65 arcmin, and the response of the instrument is very well known, CTA will be able to detect it as an extended source even if the PSF of the instrument is larger (~ 1.8 arcmin). However, it would be difficult to study substructures inside the source because the angular size of these substructures would be too small.

As far as the CTA spectrum of SNR G0.9 + 0.1 is concerned, it is shown in Fig. 7. The present analysis aims at understanding how well it is possible to recover the expected cutoff of this source. This has strong implications for the physical modelling implemented in Section 6 since a different cutoff energy could lead to inferring different physical parameters for the nebula. The spectrum has a good statistics and therefore the spectral resolution is very good. It is clearly possible to distinguish spectra with different cutoff energies. This represents a significant improvement in comparison with currently available data that does not allow to distinguish if the spectral shape of the VHE emission is a power law or a power law with a cutoff at energies higher than 20 TeV (Fig. 8).

The maximum cutoff energy detectable in the CTA simulated spectrum is $\gtrsim 100$ TeV while, for the lowest energy cutoff considered here (20 TeV), the source is detectable only up to ~ 60 TeV.

4 ASSESSING SYSTEMATIC ERRORS

The spectral analysis of the simulated data returns only the statistical errors, computed from the covariance matrix of the maximum likelihood fitting procedure. But systematic errors need to be carefully accounted for in order to assess the accuracy of the results. A fit of simulated data without considering the systematic errors will lead to

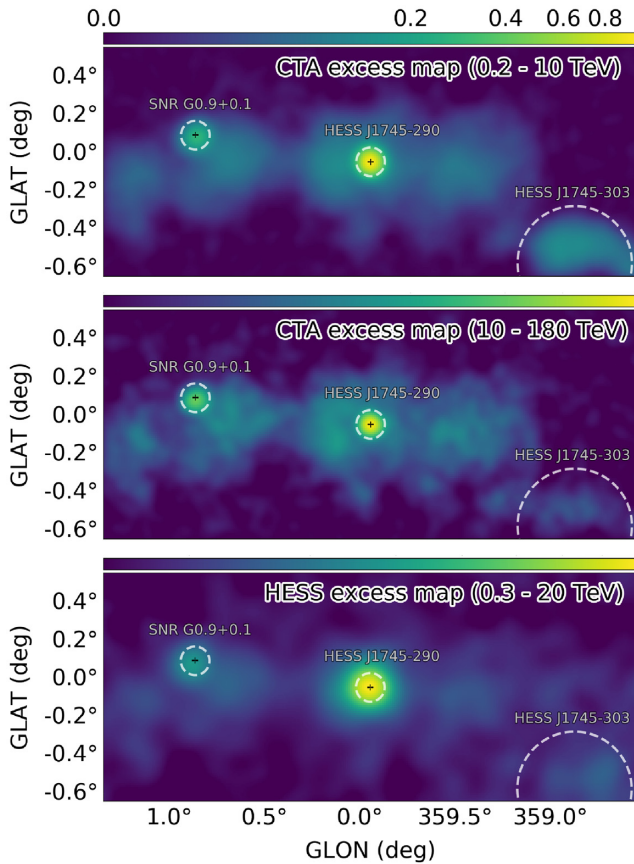


Figure 4. Simulation of the Galactic Centre-extended emission as seen with CTA in an observation of 50 h in two different energy ranges (0.2–10 TeV top panel, 10–180 TeV middle panel) and a residual map of the same region from an HESS observation in the energy range of ~ 0.3 –20 TeV (lower panel; Aharonian et al. 2006a).

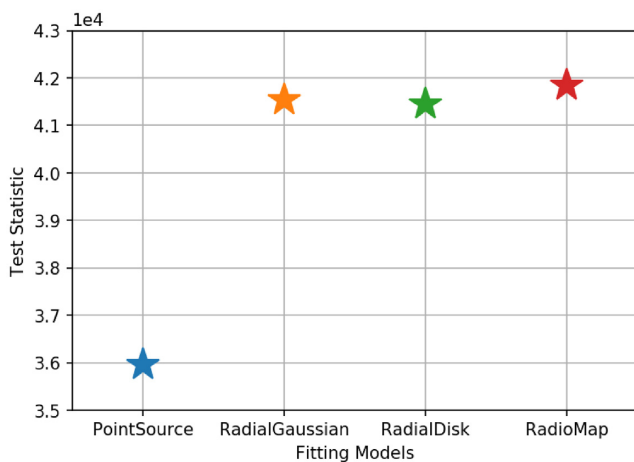


Figure 5. Test Statistics values for different fitting models applied to the simulation in which the VHE emitting region of SNR G0.9 + 0.1 is modelled with the radiomap template. The TS for the point source fitting model has a lower significance compared to the other fitting models.

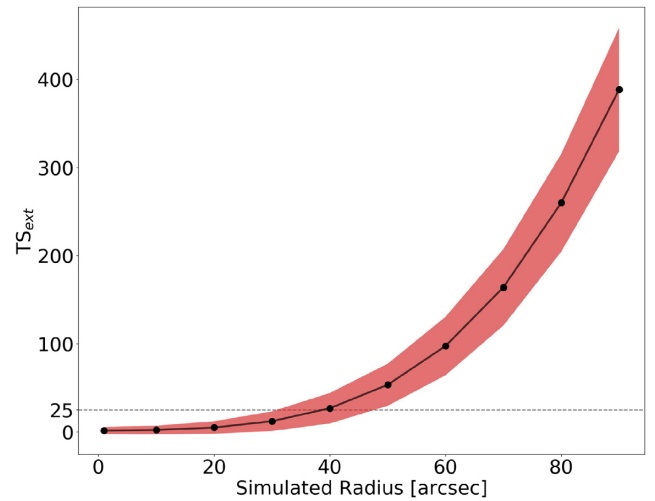


Figure 6. Significance of the detection of the source as an extended source for the images simulated using a spatially uniform radial disc with different radii. We consider $TS_{\text{ext}} \geq 25$ as the minimum value for claiming that the source is extended. The radial disc model has a significantly better likelihood when the source has a radius larger than 39^{+9}_{-8} arcsec. The red area shows the 95 per cent confidence level error region.

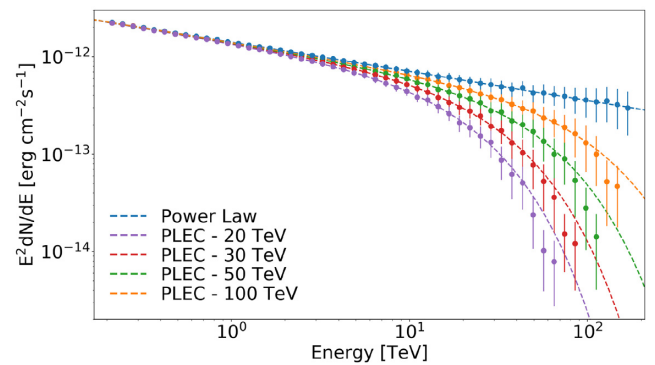


Figure 7. CTA spectral energy distribution of SNR G0.9 + 0.1, simulated using different cutoff energies. It is clearly possible to distinguish the different spectra.

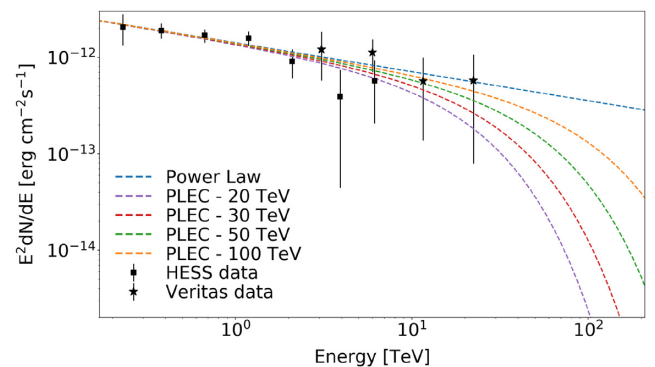


Figure 8. Comparison of the spectra simulated in this work with the data from HESS (black square) and VERITAS (black stars). With the current available data, it is not possible to rule out models with cutoff energies higher than 20 TeV.

overestimating the goodness of the fit and to results that may not be realistic.

We considered both the instrumental sources of uncertainties and the background-related uncertainties. The instrumental sources of uncertainties are due to the imperfect knowledge of the effective area and the accuracy of the reconstructed energy scale, while the background sources of uncertainties are due to the cosmic rays and the Galactic diffuse emission. In order to translate uncertainties into systematic errors on fluxes and spectral indices, we will make some assumptions on how these uncertainties propagate.

In the case of the instrumental uncertainties, we start from CTA technical requirements and we apply the following procedure to measure the associated errors.

(i) **Knowledge of the effective area.**

Uncertainty on the effective area of the system must be < 5 per cent (from the CTA technical requirements). To estimate the effect of such an uncertainty, we followed the method used by the *Fermi*-LAT team (section 5.7 of Ackermann et al. 2012). We generate perturbed IRFs that represent the worst scenario, extract the spectral parameters, and compare them to those obtained with the unperturbed IRF. The perturbed effective area A'_{eff} is written as:

$$A'_{\text{eff}}(E, \theta) = A_{\text{eff}}(E, \theta) \cdot (1 + \xi_{A_{\text{eff}}} \cdot B(E)), \quad (4)$$

where A_{eff} is the unperturbed effective area, $\xi_{A_{\text{eff}}} = 0.05$ is the uncertainty, and $B(E)$ is a function of the energy (bracketing function). Different form for $B(E)$ is adopted depending on the spectral parameter considered. For a simple power law, to maximize the effect on the normalization, the function $B(E)$ is written as:

$$B(E) = \pm 1, \quad (5)$$

while, to maximize the effects on the spectral index, the following expression is used:

$$B(E) = \pm \tanh \left(\frac{1}{0.13} \log \left(\frac{E}{E_0} \right) \right), \quad (6)$$

where E_0 is the same pivot energy used in equations (1) and (2). With these two modified IRFs, we have reanalysed the data and estimated the errors on the spectral parameters from the values obtained in the two cases.

(ii) **Accuracy of the energy scale.** The uncertainty on the energy of a photon event candidate must be < 6 per cent (from the CTA technical requirements). In order to estimate the errors on the spectral parameters induced by this uncertainty,¹³ we took the simulated data and perturbed all the photon energies as:

$$E' = E \cdot \left(1 \pm \xi_{E_{\text{scale}}} \right), \quad (7)$$

where $\xi_{E_{\text{scale}}} = 0.06$. We have then analysed these data and estimated the errors on the spectral parameters.

In the case of the uncertainties related to the knowledge of the background, we applied a different approach, as described below.

(i) **Cosmic ray background.** In order to determinate the impact of the uncertainty on the cosmic ray background, we varied its flux of ± 50 per cent¹⁴ from the nominal value. We thus changed the

¹³In this work, we have not taken into account the energy dispersion since it was computationally too expensive.

¹⁴This value is much bigger than the expected uncertainty on the residual cosmic ray background for CTA-South.

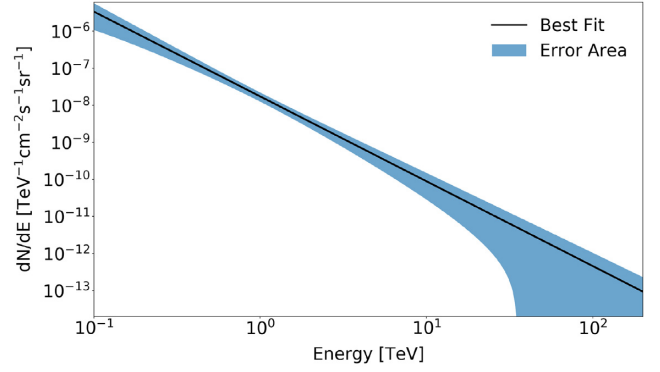


Figure 9. Average spectrum (per steradian) of the Galactic plane near the centre region (between $359.2^\circ < l < 0.8^\circ$ and $|b| < 0.3^\circ$) as measured by the HESS collaboration (Aharonian et al. 2006a). The shaded area corresponds to the error boundary of the HESS measurements, in which both statistical and systematic errors are taken in account.

normalization of the background according to:

$$N'_0 = N_0 \cdot \left(1 \pm \xi_{CR_{\text{bkg}}} \right), \quad (8)$$

where $\xi_{CR_{\text{bkg}}} = 0.5$. We then analysed these data and estimated the errors on the spectral parameters. Since the deviations from the nominal values resulting from this source of uncertainty seem to be negligible, as discussed in the next section, it was not worth considering variations induced by changes in the photon index of the cosmic ray background.

(ii) **Galactic diffuse emission.** As mentioned above, we modelled the emission from the Galactic plane central region using an HESS observation (Aharonian et al. 2006a). The best-fitting spectral model for this observation is a power law with $N_0 = 1.73 \times 10^{-8} \text{ TeV}^{-1} \text{ cm}^{-2} \text{ s}^{-1} \text{ sr}^{-1}$ and $\Gamma = 2.29$ with the associated errors $\sigma_{N_0} = (\pm 0.13_{\text{stat}} \pm 0.35_{\text{syst}}) \times 10^{-8} \text{ TeV}^{-1} \text{ cm}^{-2} \text{ s}^{-1} \text{ sr}^{-1}$ and $\sigma_\Gamma = \pm 0.07_{\text{stat}} \pm 0.20_{\text{syst}}$. Using these errors, we calculate an optimistic/pessimistic spectrum from the Galactic Centre from:

$$F_{\text{pess,opt}} = F(E) \pm \sqrt{\left(\frac{\partial F}{\partial N_0} \right)^2 \sigma_{N_0}^2 + \left(\frac{\partial F}{\partial \Gamma} \right)^2 \sigma_\Gamma^2}, \quad (9)$$

where $F(E)$ is the best-fitting value of the flux, the pessimistic case F_{pess} corresponds to the sign $+$, and the optimistic case F_{opt} to the sign $-$. This is an approximation of the error propagation formula (we lack all the information on the full covariance matrix that comes from the analysis made by the HESS collaboration). The spectrum is shown in Fig. 9. We have then analysed these perturbed data and measured the associated errors. We repeated the analysis using the pessimistic and optimistic estimate of the spectrum and used the spectral parameters of the source inferred in the two cases to estimate the errors induced by this systematic uncertainty on it. It is worth to mention that also the uncertainty on the morphology of the Galactic diffuse emission can be a source of systematics error. However, at present we, have not enough information to assess the uncertainties related to the morphology of diffuse emission. This task is left for future studies.

For all these sources of uncertainty, we have repeated the simulations 100 times and we have then taken the final errors on the average values as representative of the uncertainties induced by the different simulations.

Table 3. Systematic errors measured using the deviation of the perturbed values from the nominal ones, as explained in the text. We report for comparison also the statistical errors computed from the likelihood analysis made with ctools.

Statistical errors	N_0^a	δN_0^a	$\delta N_0/N_0$	Γ	$\delta\Gamma$	$\delta\Gamma/\Gamma$
Nominal value	8.820×10^{-13}	7.322×10^{-15}	0.830%	2.306	0.006	0.251%
Systematic errors	N_0^a	δN_0^a	$\delta N_0^a/N_0$	Γ'	$\delta\Gamma'$	$\delta\Gamma'/\Gamma$
A'_{eff} (equation (5) -5%)	9.351×10^{-13}	5.309×10^{-14}	6.019%	2.309	0.003	0.123%
A'_{eff} (equation (5) +5%)	8.334×10^{-13}	-4.865×10^{-14}	-5.516%	2.310	0.004	0.177%
A'_{eff} (equation (6) +5%)	8.846×10^{-13}	2.632×10^{-15}	0.298%	2.333	0.027	1.179%
En. scale (-6%)	8.555×10^{-13}	-2.656×10^{-14}	-3.012%	2.320	0.014	0.613%
En. scale (+6%)	9.055×10^{-13}	2.351×10^{-14}	2.666%	2.303	-0.003	-0.128%
Cosmic ray (-50%)	8.837×10^{-13}	1.668×10^{-15}	0.189%	2.302	-0.042	-0.079%
Cosmic ray (+50%)	8.882×10^{-13}	6.184×10^{-15}	0.701%	2.309	0.003	0.117%
Gal. diffuse (opt.)	8.807×10^{-13}	-1.277×10^{-15}	-0.145%	2.302	-0.004	-0.166%
Gal. diffuse (pess.)	8.807×10^{-13}	-1.315×10^{-15}	-0.149%	2.308	0.002	0.082%

Note. ^a N_0 and δN_0 in unit of $\text{TeV}^{-1}\text{cm}^{-2}\text{s}^{-1}$.

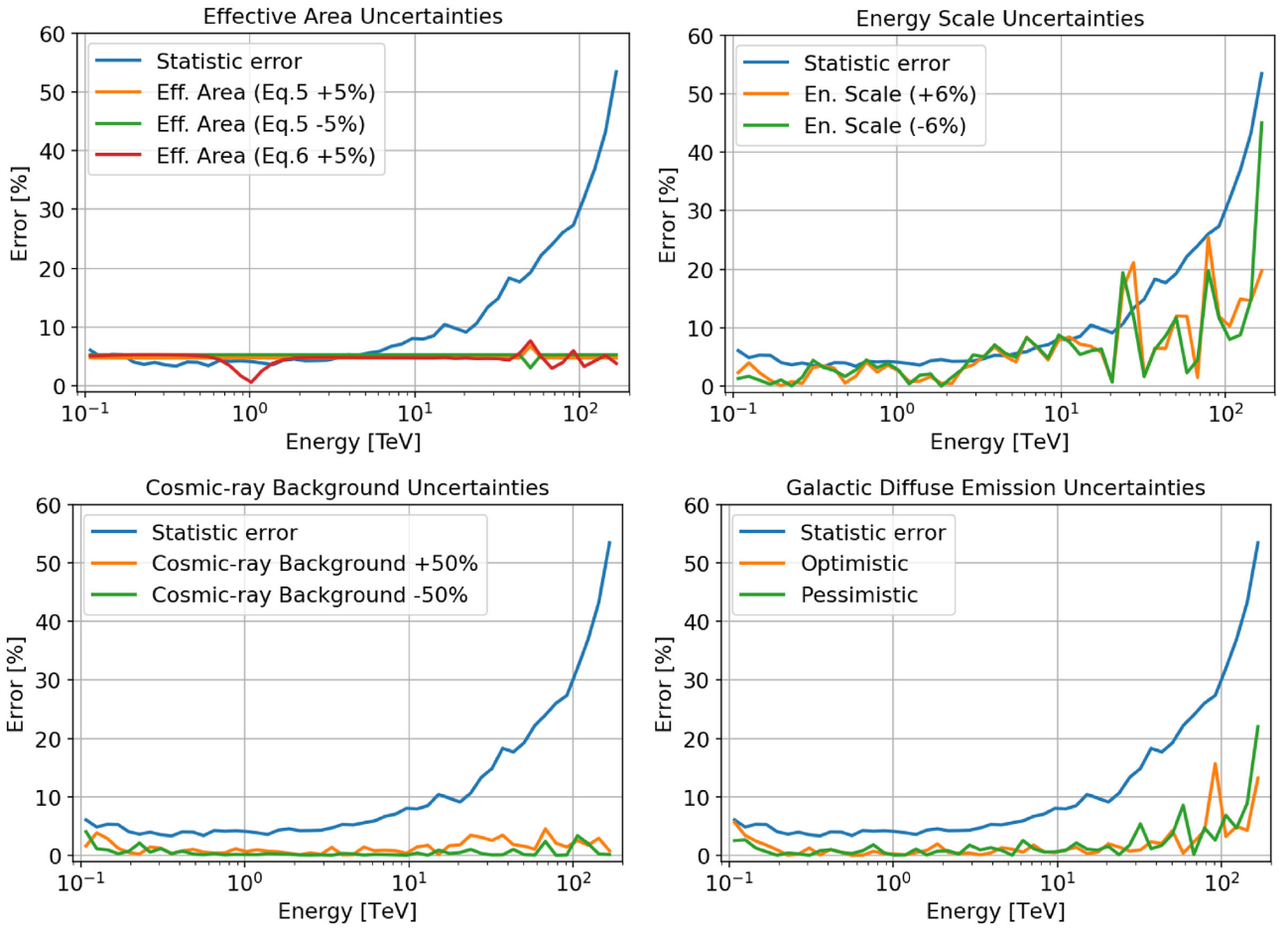


Figure 10. Fractional error on the CTA spectrum as function of photon energy, measured assuming a power-law model for SNR G0.9 + 0.1. In the low-energy range (where CTA-South will have the best sensitivity), the instrumental uncertainties are dominant, while in the higher energy range, the decrease of the sensitivity of the array leads to an increase of the statistical errors. The background-related uncertainties are very low at all energies.

5 SYSTEMATIC ERROR ESTIMATION RESULTS

In Table 3, we report the values of the systematic errors, computed from the difference between the ‘Nominal value’ (values computed without perturbing the data) and the values obtained as explained in the previous section.

The instrumental systematic uncertainties dominate over the background-related sources of error. This is shown in Fig. 10 where we plot the errors as a function of energy, assuming a power-law spectrum. While the systematics act differently at different energies, the background-related uncertainties are always small. In the low-energy range (where the array has the best sensitivity), the instrumental uncertainties dominate and are at the same level as the

statistical errors, while in the higher energy range, the decrease of the sensitivity of CTA-South leads to an increase of the statistical errors. The behaviour of the statistical error yields a good representation of the sensitivity limit of the CTA-South array.

Although the errors reported here are probably overestimated (especially the instrumental ones), this analysis provides a good clue on the order of magnitude of the expected systematic uncertainties. According to the results of our analysis, the background-related uncertainties are negligible in comparison with the other sources of uncertainty and have a small impact on the measured spectrum.

6 MODELLING THE EMISSION OF PULSAR WIND NEBULAE

PWNe are important laboratories to test the processes responsible for the acceleration of charged particles. To this end, it is crucial to compare real or simulated data with precise and physically motivated models.

Reproducing the broad-band spectrum, from the radio band up to γ -rays, of these sources, requires a dynamical model that describes the evolution of the population of the emitting electrons inside the PWN.

A one-zone time-dependent leptonic model is often adopted. In this model, the main emitting particles are a population of electrons that evolves with time and the nebula is approximated as a sphere where the electrons are uniformly distributed.

This approach has been developed by several authors (e.g. Venter & de Jager 2007; Zhang, Chen & Fang 2008; Qiao et al. 2009; Fang & Zhang 2010; Tanaka & Takahara 2010, 2011; Bucciantini, Arons & Amato 2011; Martín et al. 2012; Torres et al. 2014; Martín, Torres & Pedalletti 2016; van Rensburg et al. 2018). In this work, we follow the approach presented by Gelfand et al. (2009). We also test the results of our implementation for the PWN in SNR G0.9 + 0.1 against those obtained by Zhu et al. (2018) and Torres et al. (2014).

6.1 The model

The distribution and the evolution of the electronic population inside the nebula are described by an energy-diffusion equation. The general form of this equation [see equation (A1)] and the meaning of all the terms of the equation are described in Appendix A. The simplified form used in this work is as follows:

$$\frac{\partial N(E, t)}{\partial t} = Q(E, t) - \frac{\partial}{\partial E}[b(E)N(E, t)] - \frac{N(E, t)}{\tau_{\text{esc}}(E, t)}, \quad (10)$$

where $N(E, t)$ is the number density of the electrons, $Q(E, t)$ the injection rate of electrons at the termination shock, $b(E)$ the variation of the mean energy of the electrons per unit time, and $\tau_{\text{esc}}(E, t)$ is a characteristic time scale describing the escape of the electrons from the system.

The typical shape adopted for the injection spectrum of the particles is a broken power law. Other types of injection spectra have been proposed but all somehow fail to reproduce the observed spectrum or are difficult to motivate (see the discussion in Gelfand 2017). The broken power-law spectrum can reproduce well the different slopes of the synchrotron spectrum observed in many PWNe, as the Crab Nebula (Atayan & Aharonian 1996), in the radio and X-ray bands. We then assume (Tanaka & Takahara 2010; Bucciantini et al. 2011; Martín et al. 2012; Torres, Cillis & Martín

Rodríguez 2013; Zhu et al. 2015):

$$Q(E, t) = Q_0(t) \begin{cases} (E/E_b)^{-\alpha_1} & \text{for } E \leq E_b \\ (E/E_b)^{-\alpha_2} & \text{for } E > E_b \end{cases}, \quad (11)$$

where $Q_0(t)$ is a normalization factor determined from the fraction of the spin-down luminosity $L(t)$ of the pulsar that goes in particles energy and E_b is the break energy where the slope of the particle spectrum changes. If we write the spin-down luminosity of the pulsar in the form

$$L(t) = L_0 \left(1 + \frac{t}{\tau_0}\right)^{-\frac{(n+1)}{(n-1)}}, \quad (12)$$

where L_0 is the initial spin-down luminosity, τ_0 is the initial spin-down time-scale, and n is the braking index (Gaensler & Slane 2006), we can find the normalization factor $Q_0(t)$ from:

$$(1 - \eta_B)L(t) = \int_{E_{\text{min}}}^{E_{\text{max}}} EQ(E, t)dE. \quad (13)$$

Here, the constant η_B , the magnetic fraction of the nebula (Martín et al. 2016), is the fraction of the spin-down luminosity that goes into the electromagnetic field,¹⁵ while $1 - \eta_B$ is the fraction of the spin-down luminosity that goes in the kinetic energy of the electrons.

The escape time-scale $\tau_{\text{esc}}(E, t)$ is computed from the assumption that particles can escape from the nebula because of diffusion. This diffusion inside a PWN arises from the interaction of particles with irregularities in the magnetic field (Vorster et al. 2013). Assuming that the diffusion of plasma across the magnetic field in the PWN follows Bohm law, $\tau_{\text{esc}}(E, t)$ is given by:

$$\tau_{\text{esc}} = \frac{eB(t)R_{\text{pwn}}^2(t)}{2Ec^2}, \quad (14)$$

where R_{pwn} is the radius of the PWN.

The second term in equation (10) includes the energy variation because of synchrotron radiation, IC scattering, Self-Synchrotron Compton (SSC), and adiabatic losses (Ginzburg & Syrovatskii 1964).

The minimum energy E_{min} of the injected electrons is a free parameter in this model and we choose to select a value equal to the electrons rest mass energy (0.51 MeV). On the other hand, the maximum electron energy E_{max} has to be determined because it is strictly related to the accelerations processes at the termination shock. There are different ways to calculate E_{max} . For high magnetic field strengths (for very young PWNe), one can estimate it by balancing synchrotron losses acceleration gains (de Jager et al. 1996). For lower magnetic field strengths, one needs to consider that the highest energy particle must have a gyro-radius comparable to the shock radius to participate to the acceleration process (de Jager & Djannati-Ataï 2009). Another possibility for estimating E_{max} is to consider the electric potential of the neutron star magnetosphere (Bandiera 2008; Bucciantini et al. 2011; Granot et al. 2017) and determine the maximum energy that electrons can gain while moving through the polar cap potential. We computed E_{max} considering all three different approaches and adopted the second one because the other two yield unreasonably high values. The second condition is equivalent to impose that the Larmor radius R_L must be a fraction $\epsilon < 1$ (ϵ containment factor) of the termination shock radius R_S . The Larmor radius can be written as

$$R_L = \frac{E_{\text{max}}}{eB_S}, \quad (15)$$

¹⁵This is not to be confused with the so-called magnetization parameter $\sigma(t) = \eta_B/(1 - \eta_B)$.

and so the maximum energy becomes:

$$E_{\max} = \epsilon e B_S R_S. \quad (16)$$

Finally, we need an expression for the magnetic field at the termination shock B_S . From Kennel & Coroniti (1984), the post-shock field is expressed as:

$$B_S = \kappa \sqrt{\eta_B \frac{L(t)}{c}} \frac{1}{R_S}, \quad (17)$$

where κ is the magnetic field compression ratio taken equal to 3 (strong shock condition). The final expression for the maximum electron energy is then:

$$E_{\max} = 3\epsilon \sqrt{\eta_B \frac{L(t)}{c}}. \quad (18)$$

To compute the evolution of the magnetic field, we consider the adiabatic losses due to expansion work done by the nebula on the surroundings and the energy input from the pulsar wind (Pacini & Salvati 1973; Gelfand et al. 2009; Torres et al. 2013):

$$\frac{dW_B(t)}{dt} = \eta_B L(t) - \frac{W_B(t)}{R_{\text{pwn}}(t)} \frac{dR_{\text{pwn}}}{dt}, \quad (19)$$

where $W_B = (4\pi/3)R_{\text{pwn}}^3(t)B^2(t)/(8\pi)$ is the total magnetic energy. The integration over time of this equation leads to

$$B(t) = \frac{1}{R_{\text{pwn}}^2(t)} \sqrt{6\eta_B \int_0^t L(t') R_{\text{pwn}}(t') dt'}. \quad (20)$$

The last ingredient of the model is the dynamical evolution (radius and the expansion velocity) of the PWN. We compute it with an iterative approach that is explained in Appendix B.¹⁶

The diffusion-loss equation (equation 10) is solved using a freely available code, called GAMERA¹⁷ (Hahn 2015). Once the evolution of the particle spectrum is computed, it is possible to derive directly the photon spectrum with GAMERA. The synchrotron spectrum is computed considering an isotropic pitch angle distribution of the electrons as in Ghisellini, Guilbert & Svensson (1988). The IC emission is computed using the full Klein-Nishina cross-section (Blumenthal & Gould 1970) on a background radiation field (generally composed by the CMB photons and two infra-red components). Synchrotron Self-Compton (SSC) emission is also included (Atayan & Aharonian 1996).

6.2 Model test and comparison

The model has several parameters that constrain various physical properties of the system. Since some of them are significantly degenerate, as the distance and the age of the system, we decide to fix them by choosing reliable value as reported in the literature (age, distance, energy of the SN explosion, density of the interstellar medium, and photon background, see Table 4). In addition to these parameters, several parameters of the pulsar (spin-down luminosity, period derivative, characteristic age) are also known and are reported in Table 4. The remaining parameters are those related to the spectrum of the injected electrons population (the break energy and the two indices of the broken power law), the magnetic fraction of the nebula, and the containment factor.

¹⁶The caveats of this iterative approach are described at the end of appendix B.

¹⁷libgamera.github.io/GAMERA/docs/main_page.html

When fitting the data, we leave the injection parameters free to vary. The only exceptions are α_1 and E_b that can be constrained from the radio and X-ray data. As already stated, changing some of the fixed parameters could, in principle, lead to very different values for the fitted parameters. For example, changing the distance of the system would lead to different values for the ejected mass of the SN, the age of the system, and the densities of the background photon fields for preserving the radius and TeV flux. This would in turn lead to estimating completely different parameters for the nebula. The distance of the source must be estimated accurately to break this degeneracy. However, once the distance is fixed at a certain value, the fitted parameters are fairly well determined. In the following, we will not consider this degeneracy and we will fix the distance of the source to 13.3 kpc (as reported by H. E. S. S. Collaboration 2018b), since determining it is not the main focus of this paper. The fitting procedure and error estimation of the fitted parameters are reported in Appendix C.

We tested our implementation against the results presented in Zhu et al. (2018) and Torres et al. (2014), selecting the same set of data for consistency. The radio data are taken from Dubner et al. (2008), the X-ray data from Porquet, Decourchelle & Warwick (2003), and the current VHE data from Aharonian et al. (2005). For the X-ray data, in performing the fit, we considered only two points, one at the lower and the other at the higher bound of the energy interval (with the corresponding errors). They were computed from the best-fitting power law reported by Porquet et al. (2003). The rationale behind this choice was to avoid giving too much weight to the X-ray data in comparison with the radio data (with only three points), to sample with a similar number of points the synchrotron and the IC peaks (five and seven points, respectively), and to comparatively increase the weight of the TeV data in the following section. This is crucial to understand to what extent the better quality of the CTA data will help in estimating the parameters of PWNe.

The values of the fitted parameters and their comparison with those found in Zhu et al. (2018) and Torres et al. (2014) are reported in Table 4. Results are consistent. However, the (fixed) value of the ejected mass M_{ej} is slightly different. This difference is likely caused by differences in the approach adopted to solve equation (10). However, the discrepancy does not appear to be particularly relevant considering the actual uncertainty on the knowledge of this parameter.

We emphasize that the parameter ϵ is loosely constrained because the data do not cover the part of the spectrum where the effects of this parameter are more evident (i.e. in the high-energy tails of the synchrotron and IC peaks). It is possible to see this effect in Fig. 11 where we vary only ϵ between 0.02 and 0.98 with a constant step of 0.04. This parameter is only constrained to be >0.1 . We then took $\epsilon = 0.25$ as reference value for all the models in the subsequent analysis.

Fig. 12 shows the final best-fitting electron and photon spectra. The reduced chi square of the fit is $\chi^2_{\nu} = 1.1$.¹⁸

6.3 Fit of simulated CTA data

We applied this model of the PWN evolution to the various simulated spectra of SNR G0.9 + 0.1 reported in Section 3.2, assuming that most of the simulated VHE emission comes from the central PWN.

¹⁸The reported value of the reduced chi square is not to be intended as an absolute measurement of the goodness of the fit on the original complete data set (we did not consider all the X-ray spectral points) but only as a reference value useful for comparison with the fits of the simulated data reported below.

Table 4. Fixed and fitted parameters of the model in comparison with those of Zhu et al. (2018) and Model 2: Torres et al. 2014. Dots mean that the same value is adopted. All the parameters are computed for the estimated age t_a .

	This work	Zhu et al. (2018)	Torres et al. (2014)	Notes
Pulsar and SN parameters (fixed)				
P (ms)	52.2	–	–	From Camilo et al. (2009)
\dot{P} (s s $^{-1}$)	1.56×10^{-13}	–	–	From Camilo et al. (2009)
τ_c (yr)	5305	–	–	$P/(n-1)\dot{P}$
n	3	–	–	Fixed at the standard braking index value
$L(t_a)$ (erg/s)	4.32×10^{37}	–	–	From Camilo et al. (2009)
t_a (yr)	3000	–	–	Estimated age ^a
τ_0 (yr)	2305	–	–	$[2\tau_c/(n-1)] - t_a$
L_0 (erg/s)	2.29×10^{38}	–	–	From equation (12)
M_{ej} (M_\odot)	9	14	17	Estimated ^a
E_{sn} (erg)	10^{51}	–	–	Estimated ^a
d (kpc)	13.3	–	13.	From H. E. S. S. Collaboration et al. (2018b)
Environment parameters (fixed)				
n_h (cm 3)	0.01	–	1.	From Zhu et al. (2018)
T_{CMB} (K)	2.7	–	–	From Longair (2008)
U_{CMB} (eV/cm 3)	0.25	–	–	From Longair (2008)
T_{FIR} (K)	30	–	–	From Torres et al. (2014)
U_{FIR} (eV/cm 3)	3.8	–	–	From Torres et al. (2014)
T_{NIR} (K)	3000	–	–	From Torres et al. (2014)
U_{NIR} (eV/cm 3)	25	–	–	From Torres et al. (2014)
Injection parameters				
E_b (TeV)	0.045	–	0.026	From Zhu et al. (2018)
α_1	1.1	–	1.2	From Zhu et al. (2018)
α_2	2.523 ± 0.022	2.52 ± 0.02	2.5	Fitted
η_B	0.0313 ± 0.0055	0.029 ± 0.004	0.02	Fitted
ϵ	>0.10	0.25 ± 0.08	0.2	Fitted
PWN parameters^b				
$R_{pwn}(t_a)$ (pc)	3.46 ± 0.01	3.51	3.8	From iterative procedure in Appendix B
$B(t_a)$ (μ G)	$21.89^{+1.93}_{-2.08}$	$20.29^{+1.86}_{-1.93}$	15	From equation (20)
$E_{max}(t_a)^c$ (TeV)	>600	1452^{+600}_{-535}	971	From equation (18)

Notes. ^a t_a , M_{ej} , and E_{SN} taken in order to obtain a nebula of $\sim 2'$ located at 13.3 kpc. ^bComputed from the PWN dynamics (see Appendix B).

^cMaximum energy of the electrons in injection at the termination shock of the nebula.

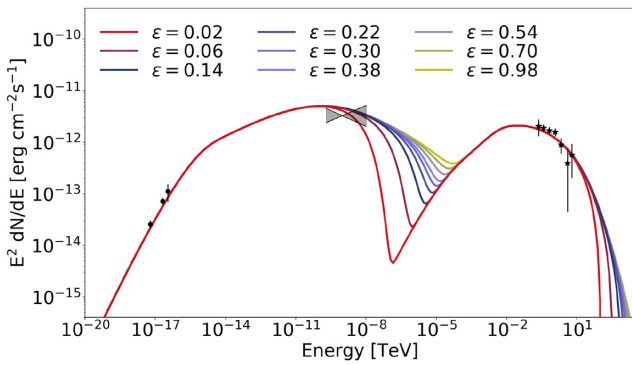


Figure 11. SED models for SNR G0.9 + 0.1 computed for $\alpha = 2.51$ and $\eta_B = 0.031$ fixed while ϵ is varying from 0.02 to 0.98 with step 0.04. We can clearly see that it is possible to rule out only really small values of the containment factor ($\epsilon \lesssim 0.1$).

The spectral range is limited at 200 GeV to be consistent with the lower limit of the HESS data and we rebin the spectrum with 10 bins. However, depending on the spectral shape, the spectrum can have less than 10 bins since at high energies, there may be no photons.

The results of the model fit are reported in Table 5, while two representative MWL spectra are shown in Fig. 13. The errors on the γ -ray data points also include the systematic errors computed in the previous section.

From Fig. 13, we see that in the lower energy part of the spectrum (the synchrotron emission peak), the model is always consistent with the data, while this is not the case at high energies.

The most interesting result is that the value of the magnetization parameters η_B is fairly well determined and tends to decrease with increasing cutoff energy, because, for energy conservation, increasing the maximum energy of the electrons requires that more power goes in particles ($1 - \eta_B$) and less in the magnetic field. In general, the MWL spectrum can constrain it.

For a cutoff at 20–30 TeV, we found a good agreement of the fitted parameters with the values obtained from the HESS data. For a cutoff at a different energy, the inferred parameters have significantly different values, which means that with the data currently available, it is not possible to accurately constrain them. With the CTA data, which have a higher energy threshold, the estimates will be more accurate. The increased sensitivity of CTA will then allow us to observe this and other PWNe at higher energies and make accurate studies on how particles are accelerated at the termination shock.

Finally, we want to emphasize that the model spectra are not consistent with a pure power-law simulated spectrum for every value of the parameters (reduced $\chi^2_\nu \simeq 2.3$). With this model, we are not able to reproduce a power law with no measured cutoff. Even changing the age and distance of the source, it is not possible to find a model that has a power-law tail up to 180 TeV. The only possibility would probably be including an hadronic component, but this is beyond the purpose of this work.

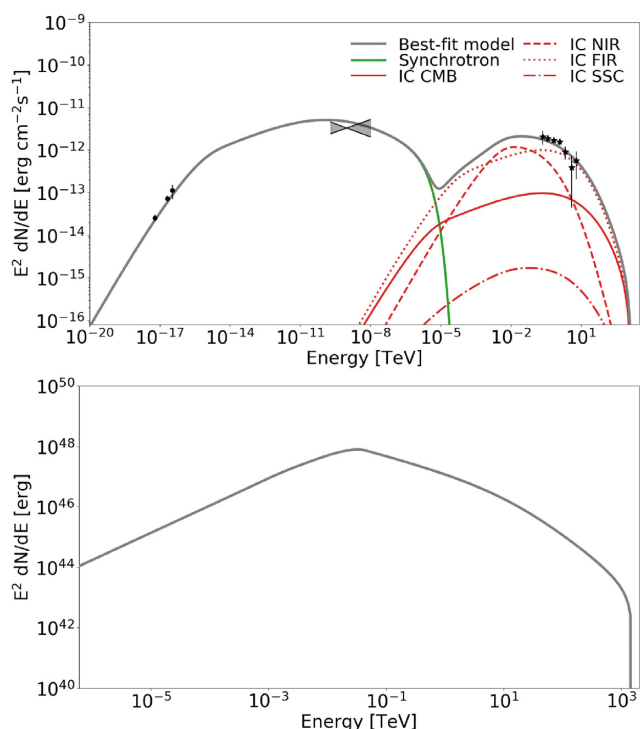


Figure 12. Photon (upper panel) and electron (lower panel) SED model for SNR G0.9 + 0.1 computed with the best-fitting values reported in Table 4. The data set is the same as in the work of Zhu et al. (2018) (more detail in the text).

6.4 Impact of the ISRF

We now try to estimate the impact on our results caused by the uncertainties on the Inter-Stellar Radiation Field (ISRF) at the (unknown) position of SNR G0.9 + 0.1. In principle, a different ISRF can affect our measurement of the parameter of the nebula since the shape of the IC component is dependent on the background radiation. In the previous analysis, we fixed the parameters of the ISRF. It would have been computationally too expensive to let them free.

The density and temperature of the near-infrared (NIR) and far-infrared (FIR) photon field can vary significantly with the position in the galaxy. Moreover, the spectral shape of this emission can be very different from the simple sum of diluted blackbodies (as assumed in the previous sections).

In order to estimate the effects of different ISRFs, we perform two different approaches. In the first, we check how much the fit differs comparing the case with fixed and free ISRF parameters. To do it, we cannot use the full model since the computational time would be too large. We then treated the dynamical evolution in a simplified way, assuming a PWN freely expanding in the SNR using just equation (B4). We then considered the CTA simulated data with a cutoff at 30 TeV and fitted them leaving α_2 and η_B free. We used a Monte Carlo Markov Chain (MCMC) code (*emcee*, Foreman-Mackey et al. 2013) and made 2500 realizations of the spectrum. We obtain results similar to those previously found ($\alpha_2 = 2.516^{+0.019}_{-0.018}$, $\eta_B = 0.0307^{+0.0052}_{-0.0050}$). After this, we repeated the fit but adding as free parameters the energy density and temperature for the IR radiation fields (T_{FIR} , U_{FIR} , T_{NIR} , U_{NIR}). We found in this case a different ISRF, with a higher energy density of the FIR component (see Fig. 14). However, the relevant parameters of the

PWN did not change significantly, although their errors increased ($\alpha_2 = 2.593^{+0.049}_{-0.041}$, $\eta_B = 0.0378^{+0.0075}_{-0.0068}$).

In the second approach, we considered a more realistic radiation field, like the axisymmetric solution for the ISFR of the Milky Way provided by Popescu et al. (2017), and used it to produce a model with fixed nebula parameters ($\alpha_2 = 2.515$, $\eta_B = 0.0315$). We selected the model reported in the first panel in fig. 9 of Popescu et al. (2017) and rescaled it by a factor of ~ 3 to obtain a similar γ -ray flux as the one of SNR G0.9 + 0.1. We then used this model to simulate an observation made with CTA, extracted the new spectrum and used it in the MCMC fitting procedure as before. We fit the usual two parameters α_2 and η_B fixing again the values for the ISRF as in the previous analysis and using two diluted blackbodies to model it. We obtained values that are in very good agreement with the ones used for the preparation of this model ($\alpha_2 = 2.524^{+0.020}_{-0.019}$, $\eta_B = 0.0321^{+0.0054}_{-0.0052}$). The results are shown in Fig. 15. We also tried to fit this model leaving all the parameters for the IR radiation field free to vary and found similar values. While the energy density of the ISRF is crucial to reproduce the IC component in the VHE spectrum, its actual spectral distribution is not, because Comptonized IR photons tend to lose rapidly memory of their initial energy.

7 CONCLUSIONS

In this work, we have studied a young PWN inside SNR G0.9 + 0.1 that is projected near the Galactic Centre. Despite the high background rate, the crowded field, and the faintness of the source, we have shown that the CTA-South array enables us to study this region and, in particular, the PWN in great detail.

In our analysis of SNR G0.9 + 0.1, we choose 200 h as observing time for the simulations in order to obtain very accurate data. This observing time is early achievable because of the projected position of this source, close to the Galactic Centre. As reported in the book ‘Science with the Cherenkov Telescope Array’ (CTA Consortium 2019), the Galactic Centre is one of the Key Science Projects for the CTA collaboration. This core programme will run for the first 3 yr of observations with CTA and will produce 525 h of data from the region of SNR G0.9 + 0.1. The 200 h of time needed for our study will be reached after ~ 1 yr after the beginning of the observations with CTA-South.

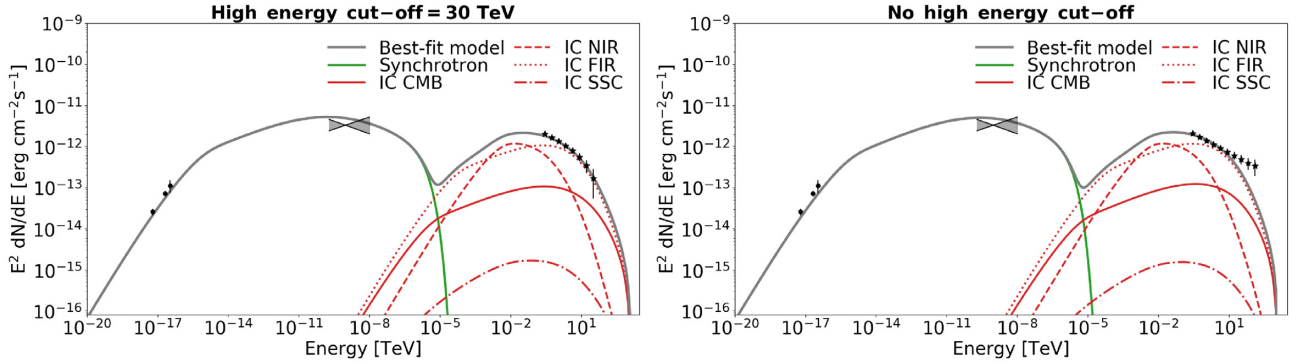
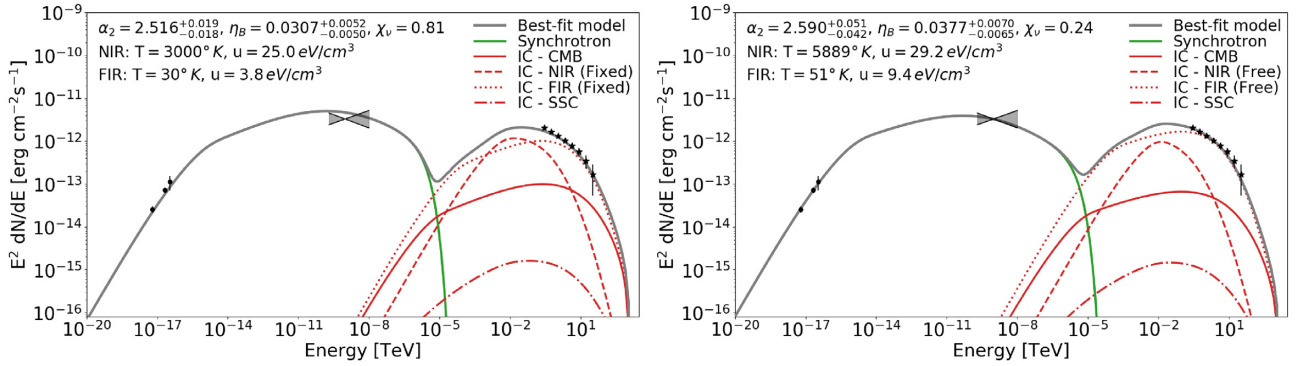
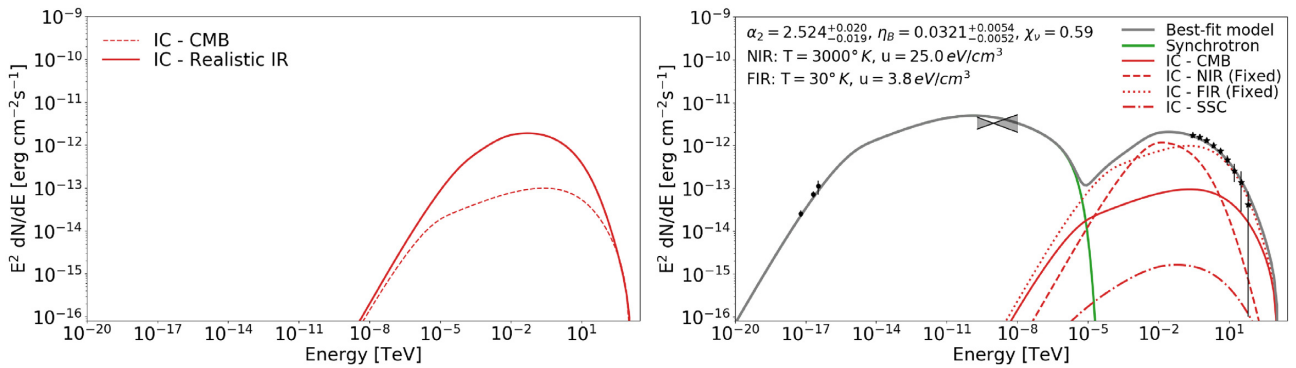
Our spatial analysis of SNR G0.9 + 0.1 shows that if the VHE emission region is larger than ~ 0.65 arcmin, CTA will be able to resolve it, leading to a measurement of the size of the nebula in the VHE band. Furthermore, our spectral analysis shows that it would be possible to distinguish different spectral models and calculate the cutoff energy, if present. We could also detect the source at energies higher than 100 TeV if the spectrum is a pure power law.

We also performed a detailed analysis of the systematic errors and found that the systematics related to the instrumental uncertainties dominate, especially at low energies. Despite these errors maybe somewhat overestimated, they provide at least an order of magnitude estimate of the uncertainties that is crucial for our subsequent analysis.

We have then implemented a one-zone time-dependent leptonic model that computes the evolution of a young PWN inside an SNR in order to obtain some physical information and to understand what impact on our knowledge of this PWN CTA may have. We first compared our result with those obtained by Zhu et al. (2018) and Torres et al. (2014) using the same data set. We find good agreement, although it is difficult to constraint the confinement factor ϵ (hence the maximum energy of the injected electrons in the nebula). Measurements of the flux of SNR G0.9 + 0.1 at MeV energies would

Table 5. Results of the fitting procedure with the PWN model adopted in this work for various CTA simulated spectra of SNR G0.9 + 0.1.

	PLEC 20 TeV	PLEC 30 TeV	PLEC 50 TeV	PLEC 80 TeV	PLEC 100 TeV	PWL
Fitting result						
χ^2_ν	0.8	0.8	0.9	1.1	1.2	2.3
α_2	2.520 ± 0.017	2.509 ± 0.016	2.507 ± 0.016	2.503 ± 0.016	2.500 ± 0.016	2.496 ± 0.016
η_B	0.0310 ± 0.0048	0.0286 ± 0.0045	0.0272 ± 0.0044	0.0257 ± 0.0042	0.0251 ± 0.0041	0.0232 ± 0.0039
R_{pwn} (pc)	3.46 ± 0.01	3.45 ± 0.01				
B (μG)	$21.81^{+1.53}_{-1.67}$	$20.97^{+1.55}_{-1.59}$	$20.44^{+1.49}_{-1.58}$	$19.87^{+1.41}_{-1.55}$	$19.65^{+1.40}_{-1.52}$	$18.89^{+1.39}_{-1.50}$

**Figure 13.** Photon SED computed with the best-fitting parameters for two out of the six different CTA simulated spectra of SNR G0.9 + 0.1 reported in Table 5.**Figure 14.** Photon SED computed with the fixed ISRF background (left-hand panel) and with the free ISRF background (right-hand panel). The best-fitting value is computed with an MCMC procedure.**Figure 15.** In the left-hand panel, we show the realistic (Popescu et al. 2017) IR background reprocessed via IC used as input for the simulation. In the right-hand panel, the photon SED fitted with just two diluted blackbodies.

be needed to obtain a precise value for this parameter. However, in the absence of MeV data, an increase of the VHE observing time would help to put constraints on the maximum electron energy because the tail of the IC peak is also sensitive to it at high energies. From the best-fitting model of the currently available data (Table 4), we expect a high-energy cutoff between 20 and 30 TeV. This is a measurement that CTA could easily do, as shown in Fig. 7, thus allowing us to reduce the uncertainties on the estimated parameters of the PWN (see Table 5).

It is worth noting that the possibility to put a constraint on the size of the VHE emission region with CTA would be crucial to check the goodness of the model, because we could compare it with the model-computed radius and to the size observed at other wavelength.

We have shown that MWL data, including CTA data (that will be capable to constrain the cutoff, if present), will lead to a more precise measurement of the magnetization parameter η_B of the nebula that, for simplicity, we considered to be constant in space and time during the evolution of the nebula. We note also that, with this model, it is not possible to reproduce a pure power-law spectrum. If detected with CTA, this would require a drastic change in the model, such as the introduction of a hadronic component.

We also checked the effects caused by uncertainties on the ISRF field. A fit leaving the ISRF parameters free leads only to small differences in the values of α_2 and η_B . Even approximating a realistic ISRF with only two diluted blackbodies, the values of α_2 and η_B are not significantly affected.

ACKNOWLEDGEMENTS

We thank the referee for his useful comments. We would also like to thank to developer of the software GAMERA, J. Hahn, for the availability at answering very quickly and clearly at our questions on the usage of the code and also for making it available to all. This paper has gone through internal review by the CTA Consortium. We made use of ctools, a community-developed analysis package for Imaging Air Cherenkov Telescope data. ctools is based on GammaLib, a community-developed toolbox for the high-level analysis of astronomical gamma-ray data. This research made use also of the following PYTHON packages: MATPLOTLIB (Hunter 2007), NUMPY (van der Walt, Colbert & Varoquaux 2011), ASTROPY (Astropy Collaboration 2013), and EMCEE (Foreman-Mackey et al. 2013). We acknowledge financial contribution from the Istituto Nazionale di Astrofisica (INAF) through grant ‘ASTRI/CTA Data Challenge (ACDC)’.

DATA AVAILABILITY

The data underlying this article will be shared on reasonable request to the corresponding author.

REFERENCES

Acero F. et al., 2010, *MNRAS*, 402, 1877
 Acharyya A. et al., 2019, *Astropart. Phys.*, 111, 35
 Ackermann M. et al., 2012, *ApJS*, 203, 4
 Actis M. et al., 2011, *Exp. Astron.*, 32, 193
 Aharonian F. et al., 2004, *A&A*, 425, L13
 Aharonian F. et al., 2005, *A&A*, 432, L25
 Aharonian F. et al., 2006a, *Nature*, 439, 695
 Aharonian F. et al., 2006b, *ApJ*, 636, 777
 Aharonian F. et al., 2008, *A&A*, 483, 509

Aharonian F. et al., 2009, *A&A*, 503, 817
 Ahnen M. L. et al., 2017, *A&A*, 601, A33
 Archer A. et al., 2016, *ApJ*, 821, 129
 Astropy Collaboration, 2013, *A&A*, 558, A33
 Atoyan A. M., Aharonian F. A., 1996, *MNRAS*, 278, 525
 Bandiera R., 2008, *A&A*, 490, L3
 Blondin J. M., Chevalier R. A., Frierson D. M., 2001, *ApJ*, 563, 806
 Blumenthal G. R., Gould R. J., 1970, *Rev. Mod. Phys.*, 42, 237
 Bucciantini N., Arons J., Amato E., 2011, *MNRAS*, 410, 381
 Camilo F., Ransom S. M., Gaensler B. M., Lorimer D. R., 2009, *ApJ*, 700, L34
 Chevalier R. A., 1977, in Schramm D. N., ed., *Astrophysics and Space Science Library*, Vol. 66, Was SN 1054 a Type II Supernova? Supernovae. Springer, Dordrecht, p. 53
 Chevalier R. A., 2005, *ApJ*, 619, 839
 Cherenkov Telescope Array Consortium, 2019, *Science with the Cherenkov Telescope Array*. World Scientific Publishing Co. Pte. Ltd.
 de Jager O. C., Djannati-Ataï A., 2009, in Becker W., ed., *Astrophysics and Space Science Library*, Vol. 357, Neutron Stars and Pulsars. Springer-Verlag, Berlin, p. 451
 de Jager O. C., Harding A. K., Michelson P. F., Nel H. I., Nolan P. L., Sreekumar P., Thompson D. J., 1996, *ApJ*, 457, 253
 de Oña-Wilhelmi E. et al., 2013, *Astropart. Phys.*, 43, 287
 Dubner G., Giacani E., Decourchelle A., 2008, *A&A*, 487, 1033
 Fang J., Zhang L., 2010, *A&A*, 515, A20
 Foreman-Mackey D., Hogg D. W., Lang D., Goodman J., 2013, *PASP*, 125, 306
 Gaensler B. M., Slane P. O., 2006, *ARA&A*, 44, 17
 Gaensler B. M., Pivovarov M. J., Garmire G. P., 2001, *ApJ*, 556, L107
 Gelfand J. D., 2017, *Radiative Models of Pulsar Wind Nebulae*. Springer International Publishing, Cham, p. 161
 Gelfand J. D., Slane P. O., Zhang W., 2009, *ApJ*, 703, 2051
 Ghisellini G., Guilbert P. W., Svensson R., 1988, *ApJ*, 334, L5
 Ginzburg V. L., Syrovatskii S. I., 1964, *The Origin of Cosmic Rays*. Macmillan, New York
 Granot J., Gill R., Younes G., Gelfand J., Harding A., Kouveliotou C., Baring M. G., 2017, *MNRAS*, 464, 4895
 H. E. S. S. Collaboration, 2017, *A&A*, 612, A9
 H. E. S. S. Collaboration, 2018a, *A&A*, 612, A1
 H. E. S. S. Collaboration, 2018b, *A&A*, 612, A2
 Hahn J., 2015, *Proceedings of Science, 34th International Cosmic Ray Conference (ICRC2015)*. The Hague, The Netherlands, p. 917
 Helfand D. J., Becker R. H., 1987, *ApJ*, 314, 203
 Hunter J. D., 2007, *Comput. Sci. Eng.*, 9, 90
 Kennel C. F., Coroniti F. V., 1984, *ApJ*, 283, 694
 Kistler M. D., 2015, preprint ([arXiv:1511.01159](https://arxiv.org/abs/1511.01159))
 Knödseder J. et al., 2016, *A&A*, 593, A1
 Lande J. et al., 2012, *ApJ*, 756, 5
 Longair M. S., 2008, *Galaxy Formation*. Springer, Berlin
 Lu F.-W., Gao Q.-G., Zhu B.-T., Zhang L., 2019, *A&A*, 624, A144
 Martín J., Torres D. F., Rea N., 2012, *MNRAS*, 427, 415
 Martín J., Torres D. F., Pedalletti G., 2016, *MNRAS*, 459, 3868
 Ostriker J. P., Gunn J. E., 1971, *ApJ*, 164, L95
 Pacini F., Salvati M., 1973, *ApJ*, 186, 249
 Popescu C. C., Yang R., Tuffs R. J., Natale G., Rushton M., Aharonian F., 2017, *MNRAS*, 470, 2539
 Porquet D., Decourchelle A., Warwick R. S., 2003, *A&A*, 401, 197
 Protassov R., van Dyk D. A., Connors A., Kashyap V. L., Siemiginowska A., 2002, *ApJ*, 571, 545
 Qiao W.-F., Zhang L., Fang J., 2009, *Res. Astron. Astrophys.*, 9, 449
 Rieger F. M., de Oña-Wilhelmi E., Aharonian F. A., 2013, *Frontiers Phys.*, 8, 714
 Sidoli L., Mereghetti S., Israel G. L., Bocchino F., 2000, *A&A*, 361, 719
 Smith A. W., the VERITAS Collaboration, 2015, *Proceedings of Science, 34th International Cosmic Ray Conference (ICRC2015)*. The Hague, The Netherlands
 Tanaka S. J., Takahara F., 2010, *ApJ*, 715, 1248

- Tanaka S. J., Takahara F., 2011, *ApJ*, 741, 40
- Tibolla O., Komin N., Kosack K., Naumann-Godo M., 2008, in Aharonian F. A., Hofmann W., Rieger F., eds, American Institute of Physics Conference Series Vol. 1085, High Energy Gamma-Ray Astronomy: Proceedings of the 4th International Meeting on High Energy Gamma-Ray Astronomy. Am. Inst. Phys., New York, p. 249
- Torres D. F., Cillis A. N., Martín Rodríguez J., 2013, *ApJ*, 763, L4
- Torres D. F., Cillis A., Martín J., de Oña Wilhelmi E., 2014, *J. High Energy Astrophys.*, 1, 31
- Truelove J. K., McKee C. F., 1999, *ApJS*, 120, 299
- van der Walt S., Colbert S. C., Varoquaux G., 2011, *Comput. Sci. Eng.*, 13, 22
- van Rensburg C., Krüger P. P., Venter C., 2018, *MNRAS*, 477, 3853
- van Rensburg C., Venter C., Seyffert A. S., Harding A. K., 2020, *MNRAS*, 492, 3091
- Venter C., de Jager O. C., 2007, in Becker W., Huang H. H., eds, WE-Heraeus Seminar on Neutron Stars and Pulsars 40 years after the Discovery. Max Planck Institut für extraterrestrische Physik, Garching bei München, Germany, p. 40
- Vorster M. J., Tibolla O., Ferreira S. E. S., Kaufmann S., 2013, *ApJ*, 773, 139
- Wenger M. et al., 2000, *A&AS*, 143, 9
- Zhang L., Chen S. B., Fang J., 2008, *ApJ*, 676, 1210
- Zhu B.-T., Fang J., Zhang L., 2015, *MNRAS*, 451, 3145
- Zhu B.-T., Zhang L., Fang J., 2018, *A&A*, 609, A110

APPENDIX A: GENERAL FORM OF ENERGY DIFFUSION EQUATION

Here, we describe in detail the energy diffusion equation used in this work, starting from its general, non-simplified form (Ginzburg & Syrovatskii 1964):

$$\begin{aligned} \frac{\partial N_i(E, \vec{r}, t)}{\partial t} = & \nabla \cdot [D_i(E, \vec{r}, t) \nabla N_i(E, \vec{r}, t)] - \frac{\partial}{\partial E} [b_i(E) N_i(E, \vec{r}, t)] \\ & + \frac{1}{2} \frac{\partial^2}{\partial E^2} [d_i(E) N_i(E, \vec{r}, t)] + Q_i(E, \vec{r}, t) \\ & - \frac{N_i(E, \vec{r}, t)}{\tau_i(E, \vec{r}, t)} + \sum_k \int P_i^k(E', E) N_k(E', \vec{r}, t) dE, \end{aligned} \quad (\text{A1})$$

$N_i(E, \vec{r}, t)$ is the number density of particles species denoted with the subscript i . The first term on the right-hand side describes the spatial diffusion of particles inside the nebula and $D_i(E, \vec{r}, t)$ is the diffusion coefficient. The second term describes the continuous energy variation due to acceleration processes and energy losses, including adiabatic, synchrotron and IC losses. The function $b_i(E)$ is the mean energy variation of the particle in unit time. The third term is related to fluctuations in this continuous variation of energy of the particles, whereas the function $d_i(E)$ is equal to the mean square of the energy variation per unit time. The term $Q_i(E, \vec{r}, t)$ is the particle injection rate, which in this case originates from the acceleration of the particles at the termination shock. The fifth term accounts for the escape of particles from the system with the characteristic timescale $\tau_i(E, \vec{r}, t)$. Finally, the last term accounts for the creation and annihilation of particles with a probability distribution $P_i^k(E', E)$ (Ginzburg & Syrovatskii 1964).

The equation (A1) cannot be easily solved. Suitable approximations are usually made. First of all, we consider only one population of particles (electrons), we neglect pair creation or annihilation, and we take only the mean value of the energy losses per unit energy, neglecting any fluctuations in the continuous energy variation. We also assume an isotropic distribution of electrons, an isotropic injection term inside the nebula, and a uniform magnetic field (no diffusion effect inside the nebula). With these approximations, we can neglect the first, the third, and the last term in equation (A1), which becomes equation (10) from Section 6.1. The escape term in equation (A1) is retained, even if we neglect the other diffusive

terms. Therefore, particles are allowed to escape from the nebula, although we do not treat in detail the diffusion process.

APPENDIX B: RADIUS AND VELOCITY EVOLUTION OF PWN

In this appendix, we describe an iterative method similar to that from Gelfand et al. (2009), which we use to compute the radius R_{pwn} and the expansion velocity v_{pwn} of the PWN in each time-step. For this, it is necessary to take into account an interaction between the SNR and the PWN expanding inside it.

First of all, we determine the properties of the ejected material between the reverse shock of the remnant and the nebula. Making a standard assumption that an inner core with initially constant density is surrounded by an outer envelope with density proportional to r^{-9} (Truelove & McKee 1999; Blondin, Chevalier & Frierson 2001; Gelfand et al. 2009), the density of the ejecta can be written as:

$$\rho_{\text{ej}}(r, t) = \begin{cases} \frac{10}{9\pi} E_{\text{sn}} v_t^{-5} t^{-3} & \text{for } r \leq v_t t \\ \frac{10}{9\pi} E_{\text{sn}} v_t^{-5} t^{-3} \left(\frac{r}{v_t t}\right)^{-9} & \text{for } r > v_t t \end{cases}, \quad (\text{B1})$$

where $v_t = (40E_{\text{sn}}/18M_{\text{ej}})^{1/2}$ is the transition velocity between the constant density core and the outer envelope, E_{sn} is an energy of the supernova explosion, and M_{ej} is its ejected mass. The ejecta during this stage is expanding ballistically and, therefore, its velocity is equal to $v_{\text{ej}} = r/t$. Since in this work we study young PWNe, which have not reached the reverse shock of the SNR yet, we are not aiming in further modelling of the ejecta.

We adopt a thin-shell approximation (Chevalier 2005), considering that the expanding PWN is surrounded by a thin shell of swept-up material.

Initial condition for our iterative procedure, which estimates the radius and the associated expansion velocity, is determined as described below. Considering the standard approximation of an isobaric bubble inside the thin shell, where the adiabatic losses are dominant, the equation of motion of the mass of the shell M_s can be written as (Ostriker & Gunn 1971; Chevalier 1977)

$$M_s \frac{d^2 R}{dt^2} = 4\pi R_{\text{pwn}}^2 \left[P_{\text{pwn}} - P_{\text{ej}} - \rho_{\text{ej}} \left(\frac{dR_{\text{pwn}}}{dt} - v_{\text{ej}} \right)^2 \right], \quad (\text{B2})$$

where ρ_{ej} , v_{ej} , and P_{ej} are computed at R_{pwn} , and P_{pwn} is the pressure inside the nebula. Since in this phase $P_{\text{pwn}} \gg P_{\text{ej}}$, we can simplify neglecting the second term in the right-hand side of the equation. From the first law of thermodynamics, we can write the following expression:

$$\frac{dE_{\text{pwn}}}{dt} = L(t) - 4\pi P_{\text{pwn}} R_{\text{pwn}}^2 \frac{dR_{\text{pwn}}}{dt}. \quad (\text{B3})$$

This equation is possible to solve in the approximation of $t_0 \ll \tau_0$ where $L(t_0) \simeq L_0$. Putting together equations (B1), (B2), and (B3), we obtain the following initial condition for the radius and expansion velocity (Chevalier 1977; Blondin et al. 2001):

$$R_{\text{pwn}}(t_0) = 1.44 \left(\frac{E_{\text{sn}}^3 L_0^2}{M_{\text{ej}}^5} \right)^{1/10} t_0^{6/5}, \quad (\text{B4})$$

$$v_{\text{pwn}}(t_0) \equiv \frac{dR_{\text{pwn}}}{dt}(t_0) = \frac{6}{5} \frac{R_{\text{pwn}}(t_0)}{t_0}. \quad (\text{B5})$$

With this initial condition, we can start the iterations, computing new radius of the PWN ($R_{\text{pwn}}(t + \Delta t)$) together with the magnetic field in the nebula $B_{\text{pwn}}(t + \Delta t)$ [equation (20)], the spin-down luminosity $L(t + \Delta t)$ (equation 12), the maximum energy of the

electrons $E_{\max}(t + \Delta t)$ (equation 18), and the density and the velocity of the ejecta at $R_{\text{pwn}}(t + \Delta t)$.

$$R_{\text{pwn}}(t + \Delta t) = R_{\text{pwn}}(t) + v_{\text{pwn}}(t)\Delta t. \quad (\text{B6})$$

As a second step, we computed the pressure inside the nebula, in order to determine the force acting on the shell and, therefore, a new value of the expansion velocity of the PWN. The net force that affects the shell is proportional to the difference between the pressure inside P_{pwn} and outside the nebula P_{ej} :

$$F_{\text{pwn}} \equiv \frac{d}{dt}(M_s v_{\text{pwn}}) = 4\pi R_{\text{pwn}}^2 (P_{\text{pwn}} - P_{\text{ej}}). \quad (\text{B7})$$

However, the second term of this expression can be neglected since it is expected that $P_{\text{pwn}} \gg P_{\text{ej}}$.

The total pressure inside the nebula is determined as a sum of the pressure of the magnetic field $P_{\text{pwn},B}$ and that of the moving electrons $P_{\text{pwn},e}$. Calculating the value of the magnetic field B_{pwn} from equation (20), we can determine the energy stored in the magnetic field:

$$E_{\text{pwn},B}(t) = \left(\frac{B_{\text{pwn}}^2(t)}{8\pi} \right) \frac{4\pi}{3} R_{\text{pwn}}^3(t). \quad (\text{B8})$$

From equation (B8), we obtain $P_{\text{pwn},B}$ as:

$$P_{\text{pwn},B}(t) = \frac{E_{\text{pwn},B}(t)}{\frac{4\pi}{3} R_{\text{pwn}}^3(t)} = \frac{B_{\text{pwn}}^2(t)}{8\pi}. \quad (\text{B9})$$

The contribution of the second component $P_{\text{pwn},e}$ can be computed solving equation (10) and extracting the total energy from the spectrum of evolved particles:

$$E_{\text{pwn},e}(t) = \int_{E_{\min}}^{E_{\max}} EN(E, t) dE. \quad (\text{B10})$$

Then, the electron pressure is found as follows:

$$P_{\text{pwn},e}(t) = (\gamma_{\text{pwn}} - 1) \frac{E_{\text{pwn},e}(t)}{\frac{4\pi}{3} R_{\text{pwn}}^3(t)} = \frac{E_{\text{pwn},e}(t)}{4\pi R_{\text{pwn}}^3(t)}, \quad (\text{B11})$$

where γ_{pwn} is equal to 4/3.

Finally, we are able to compute new expansion velocity of the nebula. If $v_{\text{pwn}}(t) > v_{\text{ej}}(t)$, the new mass of the shell becomes

$$M_s(t + \Delta t) = M_s(t) + \frac{4\pi}{3} \left[R_{\text{pwn}}^3(t + \Delta t) - R_{\text{pwn}}^3(t) \right] \rho_{\text{ej}}(t + \Delta t). \quad (\text{B12})$$

Otherwise, new mass $M_s(t + \Delta t)$ is simply equal to $M_s(t)$. The new velocity $v_{\text{pwn}}(t + \Delta t)$, which will be used for calculating the radius of PWN in the next iteration, can be found from the following expression:

$$v_{\text{pwn}}(t + \Delta t) = \frac{M_s(t)v_{\text{pwn}}(t) + \Delta M_s v_{\text{ej}}(t) + F_{\text{pwn}}(t)\Delta t}{M_s(t + \Delta t)}, \quad (\text{B13})$$

where $\Delta M_s = M_s(t + \Delta t) - M_s(t)$.

To compute an evolution of leptons using this iterative procedure, we solve advective equation (10) many times. In case of high energy losses, these computations can become time consuming. To speed

up the calculations, we put an upper limit on the magnetic field inside the nebula during the first stages of evolution of the system. We impose that magnetic field does not exceed $2000 \mu\text{G}$ during the first 5 yr and it is $< 200 \mu\text{G}$ up to 500 yr of evolution. These constraints introduce modest impact to the calculation of the radius of the source. Resulting value of the radius is < 5 per cent higher than that computed with no upper limits on the magnetic field. It is worth to mention that this approximation has been tested only for SNR G0.9 + 0.1 and may not be valid for younger sources (less than ~ 1000 yr), where an higher threshold for the magnetic field will be probably needed to better reproduce the observed data. We finally note that once the values needed to determine an evolution of the nebula are obtained, we recalculate the particle spectrum without any limit on the magnetic field. We also checked that the final photon spectrum does not differ significantly from that obtained using no upper limits on the magnetic field.

APPENDIX C: MODEL FITTING

In our fitting procedure, we first compute a grid of models spanning a large range of values of free parameters. We then compute the chi-square (χ^2) statistics for each model of the grid and the observational data and choose the best-fitting model with the minimal χ^2 . As mentioned in Section 6.2, we leave free to vary only three parameters: α_2 , η_B , and ϵ . Other two parameters E_b and α_1 are fixed to values as in Zhu et al. (2018) in order to perform comparison with their results. Finally, we estimate uncertainties of free parameters using the following procedure:

(i) We produce a three-dimensional (3D) probability grid from the χ^2 values obtained for all the models:

$$P_{3\text{D}}(\alpha_2, \eta_B, \epsilon) \propto \exp(-\chi^2/2), \quad (\text{C1})$$

(ii) and normalize it:

$$\sum_{\alpha_2, \eta_B, \epsilon} P_{3\text{D}}(\alpha_2, \eta_B, \epsilon) = 1, \quad (\text{C2})$$

(iii) We then extract the marginalized (1D) probability distribution for each parameter summing over other two parameters:

$$P_{1\text{D}}(\alpha_2) = \sum_{\eta_B, \epsilon} P_{3\text{D}}(\alpha_2, \eta_B, \epsilon), \quad (\text{C3})$$

$$P_{1\text{D}}(\eta_B) = \sum_{\alpha_2, \epsilon} P_{3\text{D}}(\alpha_2, \eta_B, \epsilon), \quad (\text{C4})$$

$$P_{1\text{D}}(\epsilon) = \sum_{\alpha_2, \eta_B} P_{3\text{D}}(\alpha_2, \eta_B, \epsilon). \quad (\text{C5})$$

(iv) Finally, using these marginalized probability distributions, we estimate the confidence interval and 1σ error for each parameter, assuming that the distributions are Gaussians.

This paper has been typeset from a \LaTeX file prepared by the author.